Physics of Plasmas ARTICLE pubs.aip.org/aip/pop

Prediction of neutral gas pressure in Wendelstein 7-X: Statistical analysis and machine learning

Cite as: Phys. Plasmas **33**, 012501 (2026); doi: 10.1063/5.0305811
Submitted: 8 October 2025 · Accepted: 11 December 2025 ·
Published Online: 2 January 2026

D. Angelis,[1,a)] F. Sofos,[1] S. Misdanitis,[2] C. Dritselis,[3] T. E. Karakasidis,[1] D. Valougeorgis,[2] V. Haak,[4] D. Naujoks,[4] G. Schlisio,[4] S. A. Bozhenkov,[4] V. Perseo,[4] and W7-X Team[b)]

AFFILIATIONS

[1]Department of Physics, University of Thessaly, 35100 Lamia, Greece
[2]Department of Mechanical Engineering, University of Thessaly, 38334 Volos, Greece
[3]Department of Civil Engineering, University of Thessaly, 38334 Volos, Greece
[4]Max-Planck Institute for Plasma Physics, Wendelsteinstrasse 1, 17491 Greifswald, Germany

[a)]Author to whom correspondence should be addressed: dimangelis@uth.gr
[b)]See author list of Grulke *et al.*, Nucl. Fusion, **64**, 112002 (2024).

ABSTRACT

The sub-divertor neutral gas pressure in relation to seven plasma parameters is predicted, based on the data of the Wendelstein 7-X OP1.2b experimental campaign, via two machine learning (ML) approaches, the extra trees (ET) and symbolic regression (SR) for the standard, high iota and high mirror magnetic configurations. To capture the changing behavior of moving from attached to detached conditions, the dataset in each configuration is divided into three clusters. Via a formal feature importance analysis, in all cases considered, the line integrated electron density is ranked as the most dominant parameter, while the heating power, followed by the radiated power, are always included in the key parameters. In the standard configuration, the coil control current has also been ranked very high. On the contrary, the center and edge temperatures and the toroidal current are of much less importance. The ET model yields nearly perfect predictions but it lacks interpretability and may struggle to generalize to unseen data. The two- and three-parameter expressions obtained by the SR model explicitly demonstrate the dependency of the neutral gas pressure on the plasma parameters and have greater potential for extrapolation to unseen estimates. Although SR predictions lag behind those of ET, they still remain very accurate. The present investigation provides valuable insight into the interconnection between the sub-divertor pressure and plasma parameters and may support the design and optimization of the particle and impurity exhaust system of W7-X and other fusion reactors, broadening the scope of ML applications in fusion.

I. INTRODUCTION

In present fusion reactor configurations, experiments are growing increasingly complex, generating vast amount of data. The need to suggest efficient analysis schemes has become essential in order to leverage the information produced and design the future experiments in less expensive and timely procedures. Data-driven machine learning (ML) methods are exploited and directed toward delivering models that can be both computationally efficient and accurate. As a branch of artificial intelligence (AI),[1] ML can take action based on decision-making processes, whether through supervised, unsupervised or reinforced learning techniques,[2] making it of greatest utility in data science and analysis tasks, as it can reassess past approaches and continuously improve the efficiency of solutions.

In the fusion research community, a variety of ML methods have been extensively employed for investigative purpose.[3] They range from architectures aiming to be guided by Ref. 4 or guide[5] simulation models to quasi-experimental data trained frameworks laying the path toward future reactors.[6] It has been shown that integrating ML models into plasma dynamics prediction may outperform traditional methods by approximately six orders of magnitude.[7] This kind of algorithms can be extra flexible in the parameter space and find interconnections not visible through a common statistical approach.

For more advanced tasks, such as image processing, deep learning (DL) techniques utilizing fully connected neural networks (FCNNs) and convolutional neural networks (CNNs) have the capacity to harness 2D and 3D spatiotemporal fields, which are mapped to image representations. Example applications of such methods in tokamaks include, among others, the employment of CNNs for the 2D turbulence image processing for the investigation of blob dynamics[8] and the analysis of thermal events via infrared movie analysis[9] and image processing.[10] In addition to that, accurate predictions of the electron density and device temperature have been achieved by harnessing spectroscopic data through a deep NN architecture.[11] Others, building on a more physically consistent approach, employ physics-informed neural networks (PINNs),[12] where they enforce physical laws to the problem's solution, by setting an ordinary or a partial differential equation as a constraint in a part of the loss function.[13] Example applications include the integration of PINNs to calculate the heat flux profiles in W7-X[13] or to learn turbulent models.[14,15] Selecting the most appropriate model is multi-facet and based on problem specific criteria, for instance, endeavors to monitor the status of reactors and predict plasma disruption events have been reported via PINNs,[16] FCNNs,[17] feedforward NNs,[18] and reinforcement learning techniques.[19]

From another perspective, the predefined output of a NN may lead to an abstract mapping between the dependent and independent parameters, which diverges from the fundamentals of explainable and generalizable AI. This is where symbolic regression (SR) finds room for applicability as it possesses the ability to create expressions that can reveal profound interconnections, clarify ambiguous relations, and provide a more physics-inspired overlook. Relevant works in magnetic confinement devices have been reported in tokamaks, for the identification of safe and disruptive operations[20] and the derivation of scaling formulas for the divertor heat load,[21] and in stellarators, for stating the scaling law of the energy confinement time[22] and the correlation of neutrals pressure with other system quantities.[23] Overall, ML techniques ranging from shallow to deep structures can provide robust predictive capabilities and aid the design and operation of experimental campaigns.[24] It is clear that fusion research has advanced by embracing the fourth paradigm of science,[25] demonstrating that investigating phenomena through ML techniques is not only feasible but also highly productive.

In fusion devices, effective neutral particle exhaust through the sub-divertor pumping system is of major importance for density control and for balancing particle input from pellet injection and gas-wall interaction. Since the particle exhaust rate is the product of the pumping speed times the sub-divertor pressure, it is evident that the neutral gas pressure should be accordingly adjusted to yield gas exhaust optimization. This issue has been extensively explored in tokamaks,[26,27] while the corresponding work in stellarators is rather limited. During the Wendelstein 7-X (W-7X) OP1.2b campaign, very low neutral gas pressure has been measured, indicating that further experimental and modeling work is needed.[28–31]

In this work, two different ML algorithms, the extremely randomized trees, also known as the extra trees (ET) model and the symbolic regression (SR) model, are applied to estimate the neutral gas pressure in the sub-divertor of W7-X, based on data of the associated plasma parameters. Extra Trees is a high-performance algorithm based on appropriately connected decision trees (DTs), where each one performs independent estimations about the target quantity and their average is the output prediction.[32] The SR model is a technique that seeks to find a mathematical expression that defines the relation between the input parameters and offers a clearer understanding of system interactions and better alignment with the physical principles.[33]

More specifically, the influence of seven plasma parameters on the neutral gas pressure p_n in the sub-divertor of W-7X is investigated for the standard, high iota and high mirror magnetic configurations. The input parameters include the line integrated electron density n_E, the heating P_{heat} and radiated P_{rad} powers, with $P_{rad}/P_{heat} \leq 0.8$, the toroidal plasma current I_{tor}, the coil control current I_{cc}, and the ion temperature at the center T_c and edge T_e of the plasma vessel. A similar investigation, employing almost the same dataset of the OP1.2b campaign, based, however, solely on the SR method, has been recently employed in Ref. 23. Here, the work is mainly based on the ET method and includes a feature importance analysis and detailed comparisons between ET predicted and experimental data. Complimentary work based on the SR method is also provided. In addition, the present plasma parameter set has been enhanced by including I_{cc}, which is expected to have a significant impact on p_n[34,35] and has not been previously considered. The effectiveness of the ET and SR methods to capture the behavior of p_n in terms of the plasma parameters is analyzed.

The rest of the paper is structured as follows: Sec. II includes data preprocessing and the ML methods: The dataset is reviewed and also analyzed by the pairwise Pearson correlation coefficients in Sec. II A, while the applied ML models are briefly described in Sec. II B. Then, in Sec. III, results are provided and discussed: In Sec. III A, a feature importance analysis via the ET model is applied to highlight the most influential plasma parameters. In Sec. III B, the ET model is employed to predict p_n, based on all, as well as on the highlighted plasma parameters and comparisons with experimental data are performed. In Sec. III C, closed form expressions of p_n are deduced, via the SR method, using the highlighted plasma parameters. A detailed and comparative analysis between the proposed ML models is presented in Sec. III D. Finally, in Sec. IV, the major outcomes are stated, and some future work directions are outlined.

II. DATA PREPROCESSING AND MACHINE LEARNING MODELS

The employed datasets of the OP1.2b experimental campaign of W7-X, are first defined and then statistically analyzed to gain some preliminary insight into the linear pairwise correlation of all involved parameters (Sec. II A). Next, the implemented two ML models, namely, ET and SR algorithms, are briefly described for clarity purpose, providing in parallel some information directly connected to the present work (Sec. II B).

A. Data overview and descriptive statistical analysis

Three subsets of the available data of the Wendelstein 7-X OP1.2b experimental campaign,[28,36–43] with electron cyclotron resonance heating and without neutral beam injection and pellet and impurity injection, are employed. They refer to the standard, high iota, and high mirror configurations at the AEI, AEH, and AEI ports, respectively, where the highest neutral gas pressure in each configuration has been measured. The datasets include the neutral gas pressure p_n and the associated plasma parameters [n_e, P_{heat}, P_{rad}, I_{cc}, I_{tor}, T_c, T_e], with the fraction of radiated power $f_{rad} = P_{rad} / P_{heat} \leq 0.8$ (partially attached conditions). These seven parameters form a physically motivated set for describing the conditions that affect the neutral gas pressure in W7-X. More specifically, the electron density n_e, as well as the heating and radiated powers P_{heat} and P_{rad}, are closely linked to the neutral gas particle and energy fluxes toward the plasma edge region and the divertor targets. Furthermore, the toroidal and control coil currents I_{tor} and I_{cc} modify the magnetic configuration and divertor strike-line positioning, which in turn affects how neutrals produced near the divertor are distributed within the sub-divertor region, while the plasma temperatures T_c and T_e reflect the local and global thermal state of the plasma, which influences how the neutral population develops near the divertor. The objective is to examine via ML, the effect of the plasma parameters on the neutral gas pressure, identify the most influential ones and provide accurate estimates of p_n, based on all plasma parameters, as well as on the most important ones. Detailed descriptions of the W7-X magnetic geometry, as well as measurement locations and strike lines positioning, may be found in previous works (e.g., Refs. 28, 29, 43, and 44).

A similar study has been recently performed in Ref. 23, where the effect of $[n_e, P_{heat}, f_{rad}, I_{tor}, T_c, T_e]$ has been examined via solely the SR method, finding that the dominant factor affecting p_n is the product of n_e times P_{heat}, raising each parameter to some power. Here, this analysis is extended by employing the ET model and quantifying the effect of each plasma parameter on p_n separately via a feature importance analysis. Furthermore, the present plasma parameter set is enhanced in the standard configuration by the addition of the coil control current I_{cc}, which is expected to be an important parameter, while f_{rad} is replaced by the radiated power P_{rad} (on the contrary to f_{rad}, P_{rad} is directly measured). Also, based on the updated datasets, the form of the SR expressions predicting p_n is reexamined. A statistical description of the implied dataset is presented in the Appendix.

A preliminary statistical insight into the pairwise behavior of all involved variables, including the behavior of the dependent variable p_n in relation to the seven independent plasma variables $[n_e, P_{heat}, f_{rad}, I_{tor}, T_c, T_e]$, is provided in Figs. 1, 2, and 3 for the standard, high iota, and high mirror magnetic configurations, respectively. In these figures, the diagonal elements are the histograms, while the elements below and above the diagonal are the scatter plots and Pearson correlation coefficients, respectively.

The Pearson coefficient for any pair of variables (x, y) measures the linear relationship between the two variables and is given by[45]

$$r_{x,y} = \frac{\sum_{i=1}^{n}(x_i - \bar{x})(y_i - \bar{y})}{\sqrt{\sum_{i=1}^{n}(x_i - \bar{x})^2 \sum_{i=1}^{n}(y_i - \bar{y})^2}}, \tag{1}$$

where $r_{x,y} \in [-1, 1]$ is the Pearson correlation coefficient, (x_i, y_i) are individual datapoints, and $(\bar{x}, \bar{y})$ are the mean values, with n denoting the number of datapoints. These coefficients are only indicative of pairwise linear dependency, with $r_{x,y} = 1$ and $r_{x,y} = -1$ indicating perfect linear positive and negative correlations, respectively, while $r_{x,y} = 0$ indicates no linear correlation (in the latter case the two variables may depend nonlinearly on each other). The pairwise Pearson correlations may assist in examining the relationship of individual parameter pairs, without considering the effect of the other involved parameters.

Based on the scatter plots in Figs. 1–3, it is seen that, in all magnetic configurations, p_n is proportional to $[n_e, P_{heat}, P_{rad}]$ and inversely proportional to $[I_{tor}, T_c, T_e]$. Also, in the standard configuration, although it is not easily observed, there is a small increase in p_n with I_{cc}. The prescribed behavior of p_n based on its scatter plots is further supported by the Pearson coefficients for all seven plasma parameters, as they stay positive for $[n_e, P_{heat}, P_{rad}]$, as well as for I_{cc} in the standard configuration and negative for $[I_{tor}, T_c, T_e]$. The dependence of p_n on the specific parameters reflects how changes in density, power, control currents, and plasma temperatures influence the neutral population near the divertor, while in the standard configuration, the weak but consistent trend with I_{cc} is aligned with the corresponding modifications of the divertor strike-line location.[28,30,43,44,46]

It is worthwhile to note that in the standard and high mirror configurations, the Pearson coefficients of (p_n, n_e) are 0.91 and 0.93, respectively, followed by the ones of (p_n, P_{heat}) and (p_n, P_{rad}), which are in the range of 0.61–0.73. On the contrary, in the high iota configuration, the Pearson coefficients of all three pairs, (p_n, n_e) (p_n, P_{heat}), and (p_n, P_{rad}), are in the range of 0.74–0.79. Previous experimental and theoretical works in W7-X indicate almost linear scaling between the sub-divertor neutral number density and the line integrated electron density.[30,46] Thus, considering that the neutral gas pressure is proportional to the neutral number density, the Pearson coefficients of (p_n, n_e), which are close to one, in the standard and high mirror configurations, indicating a close to linear correlation, are, to certain extend, justified. However, this is not the case in the high iota configuration, where the lower values of the Pearson coefficients indicate that the correlation becomes nonlinear, which may be in accordance with the observed higher neutral gas pressures.

Concerning the pairwise relationships between the independent plasma variables, it is useful to add that in all three magnetic configurations proportional correlations exist in the pairs (n_e, P_{heat}), (n_e, P_{rad}), (P_{heat}, P_{rad}), and (T_c, T_e), while inversely proportional correlations are observed in the pairs (n_e, T_c), (n_e, T_e), (P_{rad}, T_c), and (P_{rad}, T_e). In the standard configuration, I_{cc} increases with $[n_e, P_{heat}, P_{rad}]$ and decreases with $[I_{tor}, T_c, T_e]$. The remaining variable pairs do not exhibit a consistent trend, making it difficult to draw definitive conclusions. Nevertheless, this preliminary analysis indicates how the plasma conditions relate to the neutral gas pressure and provides a useful context for interpreting the more detailed feature-importance analysis and machine learning predictions presented in Sec. III.

Overall, Figs. 1–3 provide pairwise correlations between all variables, which are useful in the physical interpretation of the effect of each plasma parameter on the neutral gas pressure and in its estimation, via the ML methods, in the whole range of $f_{rad} \in [0, 0.8]$. However, as the plasma discharges transition from attached ($f_{rad} = 0$) to detached ($f_{rad} \to 1$) conditions, a corresponding change of the effect of the plasma parameters on p_n has been observed.[28] Thus, in Ref. 23, in order to capture this behavior and accurately predict the neutral gas pressure, the data are split into subregions with respect to f_{rad}. A formal f_{rad}-based clustering approach has been applied to identify three distinct regions in each of the three magnetic configurations with similar characteristics, allowing each one to be analyzed and modeled separately. It has been found that clustering-based predictions capture more efficiently the behavior of pressure, while applying the entire f_{rad} range can lead to misleading results, primarily due to the uneven distribution of data points with respect to f_{rad}. In light of this, and in order to have a robust comparison, on the same basis, between the present results and corresponding ones in Ref. 23, the previously proposed clusters for all three magnetic configurations are adapted. Details of

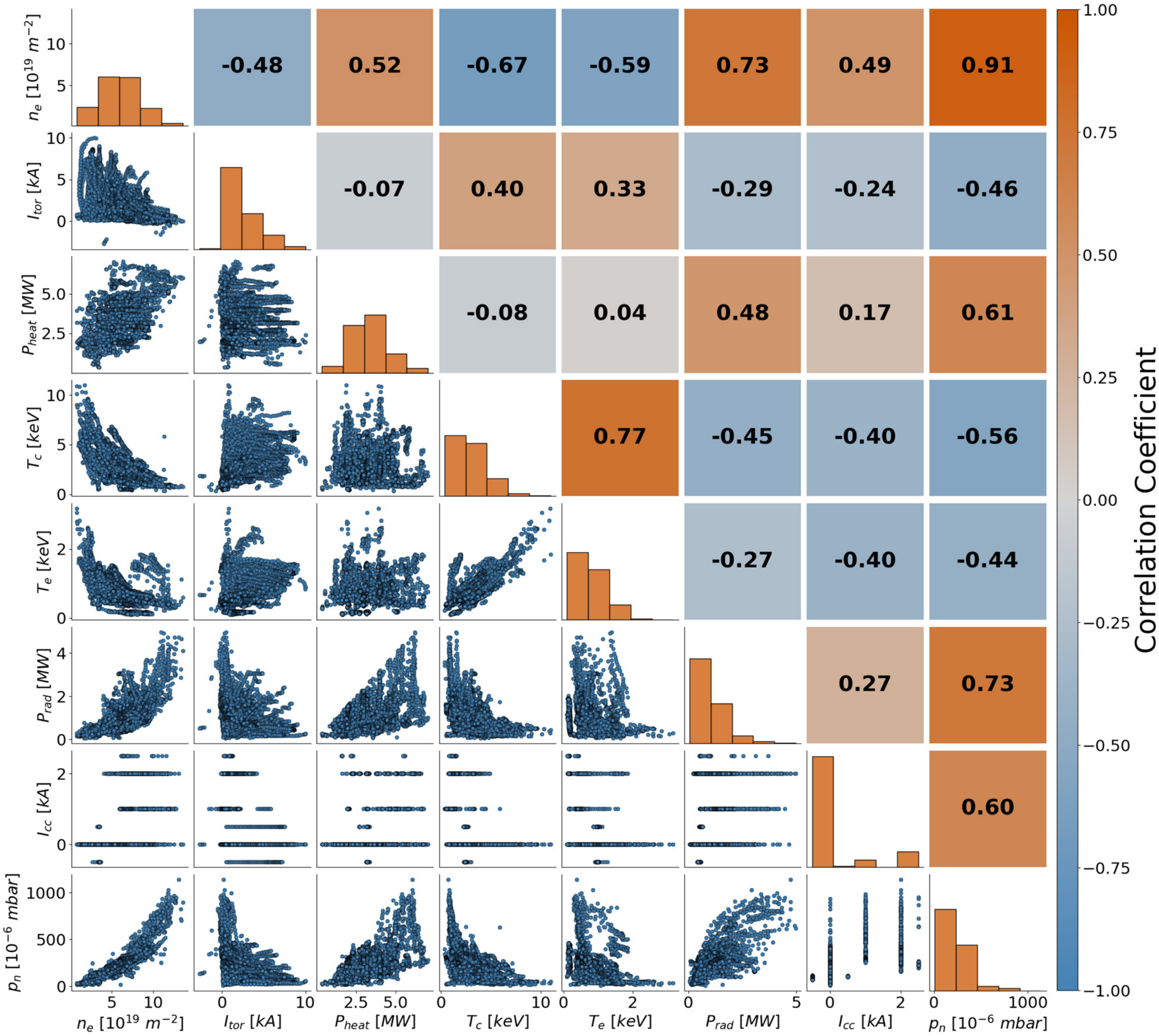

FIG. 1. Dataset characteristics of the standard configuration (AEI port) - diagonal elements are the histograms and the elements below and above the diagonal are the scatter plots and Pearson correlation coefficients respectively.

the datasets (basic statistics of all variables) are provided in the Appendix (Tables IV–VI). Thus, totally nine datasets (3 magnetic configurations $\times$ 3 clusters of f_{rad} per configuration) are considered and the two ML methods are applied in each of the nine datasets.

B. Machine learning models

Two of the most prominent tree-based ML models are employed in the present work, namely, the extra trees (ET) and symbolic regression (SR) models. A block diagram of their tree-based function is given in Fig. 4. The former leverages common decision tree features, but takes it one step further by introducing extreme randomization. The latter, even though it uses a tree-based structure to deduce the results, it does not follow a hierarchical decision-making process. Instead, it transforms the tree nodes to mathematical operators, and when connected by branches, they form symbolic expressions that can lead to more interpretable results.

The proper selection of training and testing datasets is crucial to the overall performance of the framework. The lack of generalization in a ML model is a common issue known as overfitting and its mitigating is a crucial aspect of model development, enhancing their capacity to perform effectively on real-world tasks. Here, each one of the nine datasets is split by a 70–20–10 percent factor,[23] where 70% of data points are used for training, 20% for validation purpose and the final

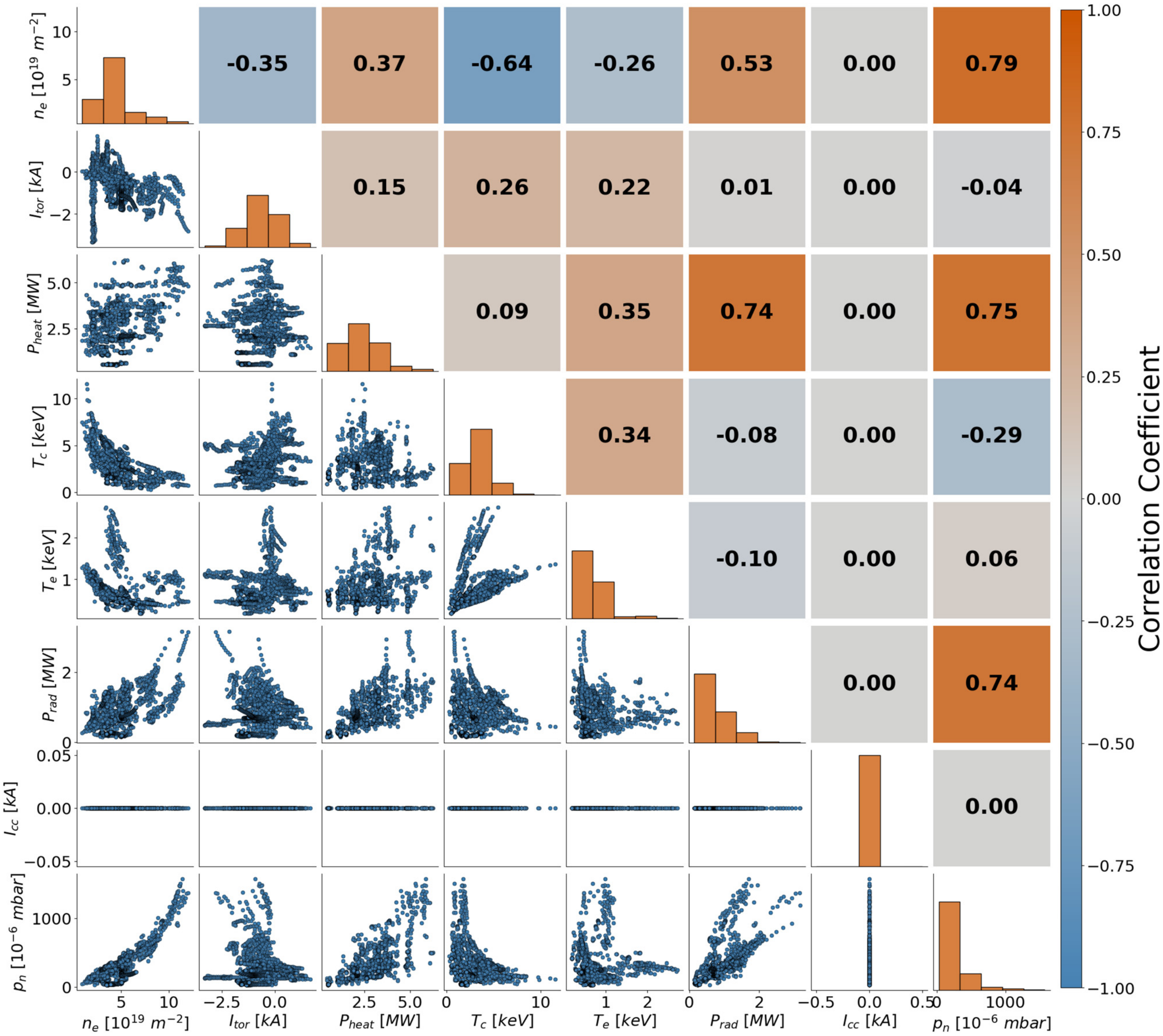

FIG. 2. Dataset characteristics of the high iota configuration (AEP port) - diagonal elements are the histograms and the elements below and above the diagonal are the scatter plots and Pearson correlation coefficients respectively.

10% is set aside and remain untouched by the ML models, as it is reserved for evaluating accuracy. Furthermore, to evaluate the predictive capabilities of the ML models, two statistical measures of accuracy are employed. They include the coefficient of determination R^2, given by[47,48]

$$R^2 = 1 - \frac{\sum_{i=1}^{n} (y_i - \hat{y}_i)^2}{\sum_{i=1}^{n} (y_i - \bar{y})^2}, \tag{2}$$

and the average absolute deviation (AAD), defined by[49]

$$AAD = \frac{1}{n}\sum_{i=1}^{n} |y_i - \hat{y}_i|, \tag{3}$$

where y_i and $\bar{y}$ refer to the experimental values and their mean, while $\hat{y}_i$ denotes the predictions of the ML model. Generally, $R^2 = 1$ shows perfect prediction, while $R^2 = 0$ suggests that the predicted $\hat{y}_i$ values are equivalent to $\bar{y}$, implying that the dependent variable (neutral gas pressure) is unaffected by the independent variables (plasma parameters).

1. Extra trees

Tree-based computational frameworks fall under the supervised learning category in ML, where the outcome is known. Their most

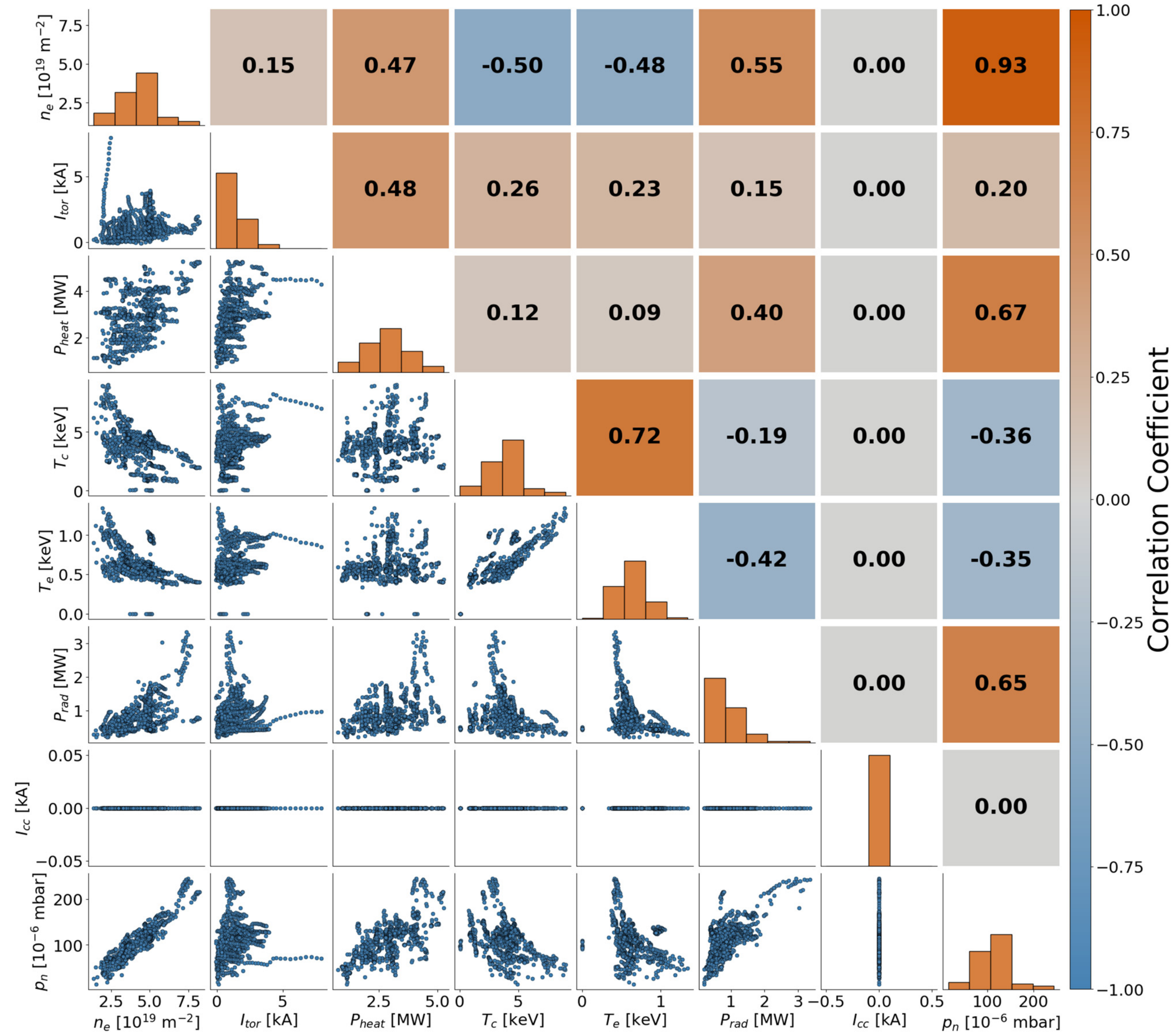

FIG. 3. Dataset characteristics of the high mirror configuration (AEI port) - diagonal elements are the histograms and the elements below and above the diagonal are the scatter plots and Pearson correlation coefficients respectively.

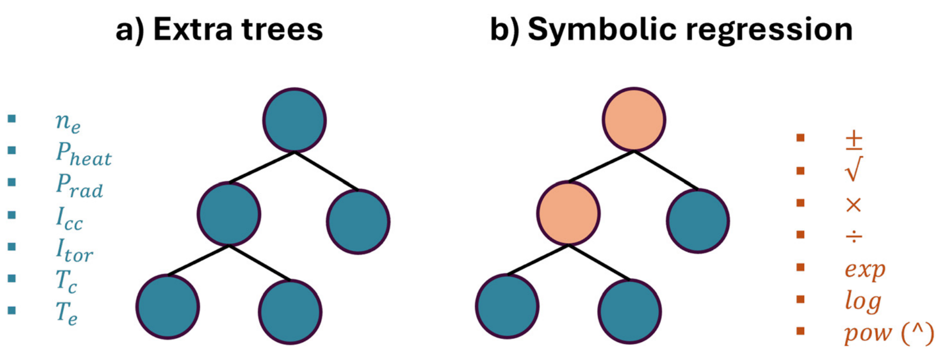

FIG. 4. The tree-based structure of (a) extra trees and (b) symbolic regression frameworks.

well-known implementation, the decision tree (DT), structures data into a tree-like model consisting of nodes and branches. Tree nodes represent a test on the data that can either be used for classification or regression tasks, while tree branches correspond to the test outcome and ultimately guide the decision-making process toward the best solution. When designing a DT, overfitting issues are common to appear, as they often arise from an excessive number of tree levels or a small number of observations reaching a terminal node.[50] For that reason, several variations of DTs are widely used.[51]

Extremely randomized trees, or extra trees (ET),[32] are an extension of the random forest algorithm, but even more random. The ET algorithm creates a large set of decision or regression trees that undergo no simplification or pruning. When compared to other conventional tree structure algorithms, one might find two main differences: First, they utilize the entire data to build trees, and second, they introduce an additional randomness to the algorithm evolution by randomly selecting both the feature and split value at the node-splitting step. These characteristics help ET to become less susceptible to overfitting and achieve better overall performance.[52] To further mitigate the overfitting issues, a repeated k-fold cross validation is employed. In k-fold cross validation,[53] the dataset is partitioned into k-subsets of equal size. Then, the algorithm uses the k-1 subsets to be trained on, and evaluate its performance on the one dataset that has not been used. It repeats the procedure k times and it estimates the final accuracy by the average performance metrics of the unseen folds. Due to the fact that the above procedure highly depends on the selected random state, a repetition into n-times provides a more reliable assessment of the performance across multiple splits. In the present work, the procedure has been repeated ten times ($n = 10$) across five folds ($k = 5$) and no signs of overfitting were observed.

2. Symbolic regression

Symbolic regression (SR) is a ML-based procedure for the extraction of a symbolic expression, capable of describing a given dataset, up to a certain extent. Among the various approaches for implementation,[33] the most prominent involve integrating features of genetic programming (GP).[54] This type of algorithms, exploit a tree-based structure to translate the outcome to a symbolic form. In contrast to DTs, in symbolic expression each node represents a mathematical operator (e.g.,$+$, $-$, $\div$, $\times$, pow) or function (e.g., $\exp(x)$, $log(x)$), which are connected via branches to materialize the final expression. By searching different combinations between features to achieve optimal results, it does not provide a single outcome. Instead, it proposes a pool of expressions usually with a ranging complexity.

The key advantage of SR over conventional, non-interpretable ML models is its ability to provide a clear and direct correlation between input parameters, without the need to account for prior knowledge as it is data-driven. This, in turn, can facilitate the better understanding of feature interactions and offer a practical guide to focus on key areas. However, the dimensionality of the input space has to remain relatively small,[55] since high dimensionality data return a very large search space, and this in turn, may yield a vast number of candidate equations of increased complexity.[51]

For the SR implementation, the framework is based on the open python-julia software PySR[56,57] and our own python code. The expression optimization process is carried along with an estimation of the expression complexity, which is analogous to the number of nodes used in the tree-structure, and the mean squared error based on the loss function, given by[58]

$$MSE = \frac{1}{n}\sum_{i=1}^{n}(y_i - \hat{y}_i)^2, \tag{4}$$

where y_i and $\hat{y}_i$ refer to the experimental and prediction values of the dependent variable. Furthermore, a series of runs are performed, each one at a different random state. The goal is to find a form of symbolic expression that remains robust to the variations in the training data, enhancing their generalization ability. The form of the final proposed expression should keep reappearing despite the randomness on GP and also should achieve high accuracy metrics.

Clearly, PySR may not export the perfect expression, but it provides a set of potential expressions drawn from a set that seems infinite.[59] To address this issue, an additive optimization step, using SciPy's minimize[60] with method set to "L-BFGS-B" and an MSE loss function is introduced, while an exponential boundary to restrict the search to positive values only is applied. Moreover, to obtain a comprehensive understanding of the potential true values, a 95% bootstrap confidence interval for each of the optimized parameters is calculated. That process is carried out using only the training dataset. Each one of the optimized values for the constant parameters and exponents of the selected expression are given in the format $X_{Lower\ bound}^{Upper\ bound}$, where X denotes the mean of the confidence interval.

Finally, to account for interpretability and overfitting issues, simple expressions are prioritized (complex functions are more likely to lead to overfitting[61,62]). The confidence in avoiding overfitting is further enhanced by evaluating the consistency of accuracy metrics across the training, validation, and test datasets. As with the ET algorithm, the SR expressions show no signs of overfitting.

III. RESULTS AND DISCUSSION

Nine different subsets referring to the standard, high iota and high mirror magnetic configurations with three cluster in terms of the fraction of radiated power f_{rad} are considered and the corresponding neutral gas pressures are predicted via the ET and SR models. The former one can capture complex inter-dependencies between the system variables, while on the contrary, the latter one seeks to reveal the underlying mechanism that generates the final pressure value by linking the independent variables to form an expression. The ML model accuracy is interpreted through its identity plots, where the predicted values $\hat{y}_i$ are plotted on the y-axis, vs the experimental ones y_i on the x-axis. The predictions are improved as R^2 increases and AAD decreases.

Given that the two ML models operate differently, in Sec. III A, a feature importance analysis is presented to identify the most influential plasma parameters on the estimation of the neutral gas pressure. This is based on the ET predictions, due to its ability to capture, in a straightforward manner, the inter-dependencies between p_n and each of the involved independent variables. Then, in Sec. III B, the accuracy of the ET algorithm is evaluated on two different occasions: first, by considering every available parameter to estimate p_n and second, by using only the key features. Next, based on these results, in Sec. III C, the SR procedure is applied to derive expressions that link the dependent variable to the dominant independent variables. Finally, in Sec. III D, a comparison between the ET and SR models is performed.

A. Feature importance analysis and identification of the key plasma parameters

The employed datasets are statistically analyzed by a feature importance analysis, via the SHapley Additive exPlanations (SHAP) approach, which may explain the output of any ML model.[63–65] The so-called SHAP value is an importance value of each input parameter and represents the effect of including this specific parameter in the ML model. In the present framework, SHAP values are obtained for each of the input (independent) variables in the plasma parameter set [n_e, P_{heat}, P_{rad}, I_{cc}, I_{tor}, T_c, T_e] and represent the importance of including the corresponding input variable in the prediction of p_n.

Figure 5 presents the feature importance plots based on the SHAP values for the ET algorithm for each of the three clusters of the standard, high iota and high mirror configurations. In the y-axis the ranking of the input plasma parameters is outlined, in descending order, measured by the mean absolute SHAP value, given in a square bracket [·], vs the corresponding SHAP value for each data point in the x-axis. The color of each point on the graph represents the value of the corresponding parameter, with red and blue indicating high and low values, respectively. Each point represents a row from the original dataset, where, relative to the mean prediction, positive SHAP values for a feature indicate it pushes the prediction higher than the mean,

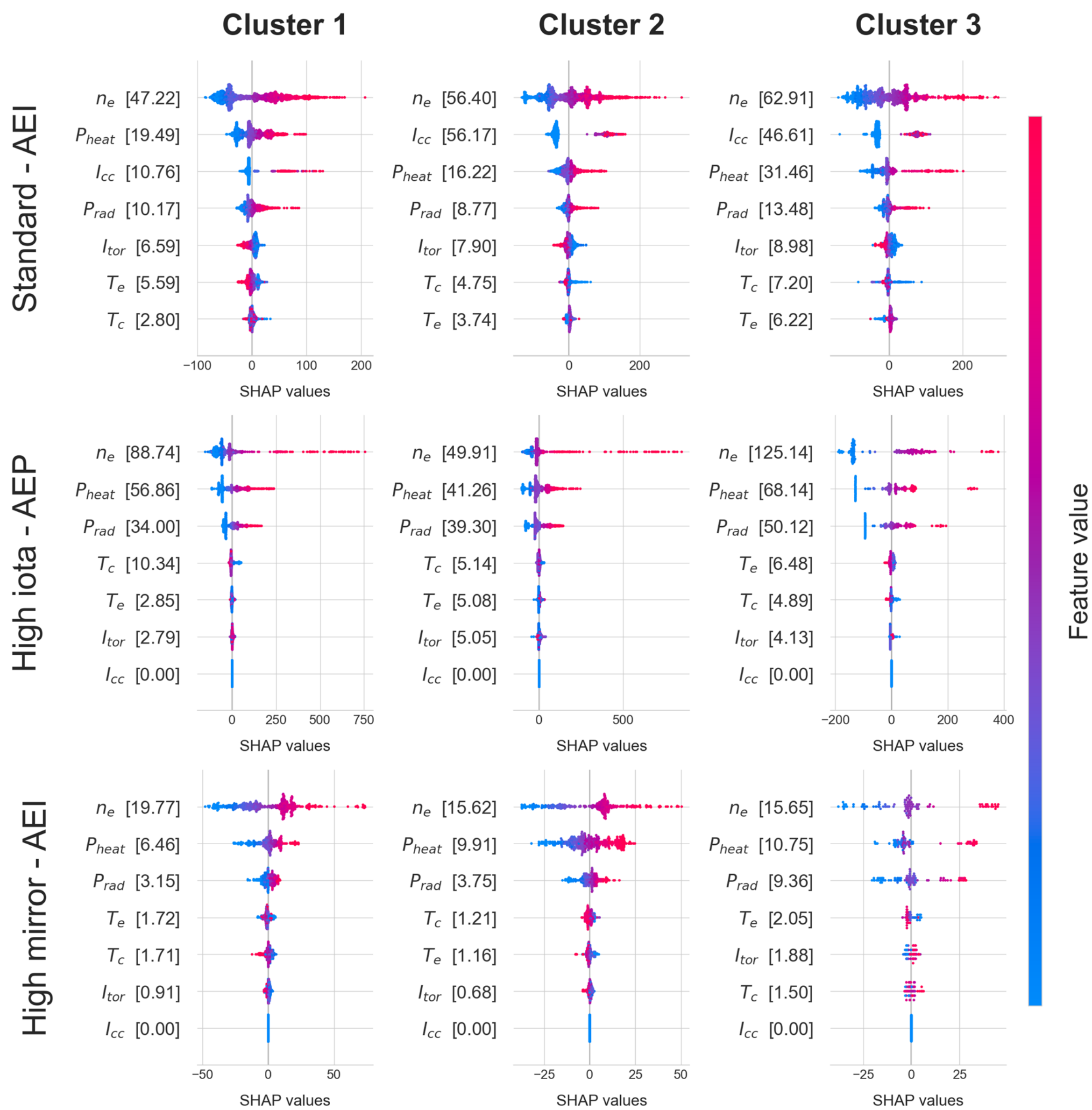

FIG. 5. SHAP value plots of the ET algorithm, for each magnetic configuration and cluster; the y-axis shows the ranking of input plasma parameters, measured by the mean absolute SHAP value, in the square brackets [·]), while the x-axis displays the SHAP value of each data point.

and negative values indicate it pushes the prediction lower. For example for the standard configuration and cluster 1, the red and blue data points of n_e indicate values close to the maximum and minimum ones respectively, as they are defined in Table IV (max $n_e = 10.58 \times 10^{19}$ m^{-2}, min $n_e = 0.82 \times 10^{19}$ m^{-2}). Input parameters at the top of the list are expected to have higher influence on the final estimation of the model, than the ones at the bottom, as the final ranking is based on the mean absolute SHAP value.[66]

The electron density n_e is ranked in clusters 1 and 3 of the standard and high iota, as well as in all clusters of the high mirror configurations, clearly as the most important input parameter. Of course, in each of these cases the distance between n_e and the second important input parameter may vary, but it always remains significantly large. In cluster 2 of the standard and high iota configurations, n_e remains in the top, but it is followed in the former case, very closely, by I_{cc} and in the latter one, not as closely, by P_{heat} and P_{rad}. Actually, based on the mean absolute SHAP values, it may argue that in all magnetic configurations, the set of influential plasma parameters include, in addition to n_e, the heating and radiating powers P_{heat} and P_{rad}, as well as the coil control current I_{cc} in the standard configuration. In all cases, the importance of P_{heat} is larger than that of P_{rad}, while the importance of I_{cc} clearly surpasses the importance of P_{heat} in clusters 2 and 3 of the standard configuration. The mean absolute SHAP values of the remaining input parameters T_c, T_e and I_{tor}, although in some cases are close to the ones of P_{rad}, always remain smaller. The preliminary correlations between the neutral gas pressure and the plasma parameters, obtained in Sec. II A, based on the Pearson coefficients, are in qualitative agreement with the present feature importance results.

Based on the above, in Table I, the most important input parameters in each magnetic configuration and cluster, with their mean absolute SHAP values, are provided. Although there are no strict threshold SHAP values in order to include and exclude some parameter, in the high iota and high mirror configurations, the mean absolute SHAP values of the selected parameters [n_e, P_{heat}, P_{rad}] are several times larger compared to the not selected ones and therefore their inclusion is statistically clearly justified. In the standard configuration, the selection is not as straightforward, but for uniformity purpose and considering that it is better to add rather than to omit some parameter, in all three clusters the selected parameters are [n_e, P_{heat}, P_{rad}, I_{cc}]. The influential sets of parameters will be employed, with different objectives, in Secs. III B and III C.

TABLE I. Most important parameters in each magnetic configuration and cluster with their mean absolute SHAP values in brackets.

Standard configuration - AEI port				
Cluster	n_e	P_{heat}	P_{rad}	I_{cc}
1	[47.22]	[19.49]	[10.17]	[10.76]
2	[56.40]	[16.22]	[8.77]	[56.17]
3	[62.91]	[31.46]	[13.48]	[46.61]
High iota configuration - AEP port				
Cluster	n_e	P_{heat}	P_{rad}	
1	[88.74]	[56.86]	[34.00]	
2	[49.91]	[41.26]	[39.30]	
3	[125.14]	[68.14]	[50.12]	
High mirror configuration - AEI port				
Cluster	n_e	P_{heat}	P_{rad}	
1	[19.77]	[6.46]	[3.15]	
2	[15.62]	[9.91]	[3.75]	
3	[15.65]	[10.75]	[9.36]	

It should be noted that although the SHAP approach identifies the most important parameters, relying solely on the data measurements and the selected ML model, the results are in agreement with previous theoretical and experimental approaches.[29,46] For example, the strong dependency of p_n on n_e and P_{heat} is well-expected, based on physical principals, while its high dependency on I_{cc} may also be explained since the positioning of the strike lines with regard to the divertor gap openings are affected by I_{cc}. Also, in the high iota configuration, the SHAP approach ranks I_{tor} as the most unimportant parameter, which can be justified, as in this configuration the particle flow rates are significantly slower than in the standard one. Overall, the present statistical analysis may support the physical interpretation of the effect of plasma parameters on the neutral gas pressure.

B. Predicted neutral gas pressure via the extra trees approach

The neutral gas pressure p_n is predicted based on all seven plasma parameters and then validated the deduced set of influential parameters, obtained in Sec. III A, by predicting again p_n, using only the important parameters. In Figs. 6 and 7, identity plots, trained on all input parameters and only on the important ones, respectively, are provided for the ET predictions in the standard, high iota and high mirror configurations, accordingly grouped in their perspective f_{rad} clusters. Training, validation and test data points are distinguished by the different shapes and colors. In each case, the corresponding R^2 and *AAD* values of the test dataset are displayed. The associated residual plots, i.e., the experimental minus predicted values $(y_i - \hat{y}_i)$ are also provided in the bottom right corner of each subfigure to illustrate the discrepancy and to offer a visual representation of the points used to calculate *AAD*.

In all cases, either using all parameters or only the most influential ones, the ET algorithm performs extremely well, consistently yielding strong statistical measures of accuracy. In the former case (Fig. 6) the reported values of R^2 are in the high iota configuration 0.996–0.997, which are considered as almost perfect, in the standard configuration 0.989–0.995 and in the high mirror configuration 0.983–0.987. The small deterioration observed in the high mirror case is mainly contributed, to the relatively small size of the dataset and the relatively low values of measured pressures (Table III). In the latter case (Fig. 7), the corresponding values of R^2 are 0.993–0.995, 0.985–0.987 and 0.960–0.974. The reduction of R^2 from the former to the latter case is considered as marginal. Similarly, as seen in Figs. 6 and 7, the associated increase in *AAD* is very small. These observations clearly demonstrate that the ET model provides very reliable predictions of the neutral gas pressure, based either on all or important parameters and thus, the set of key parameters in each magnetic configuration, is properly selected.

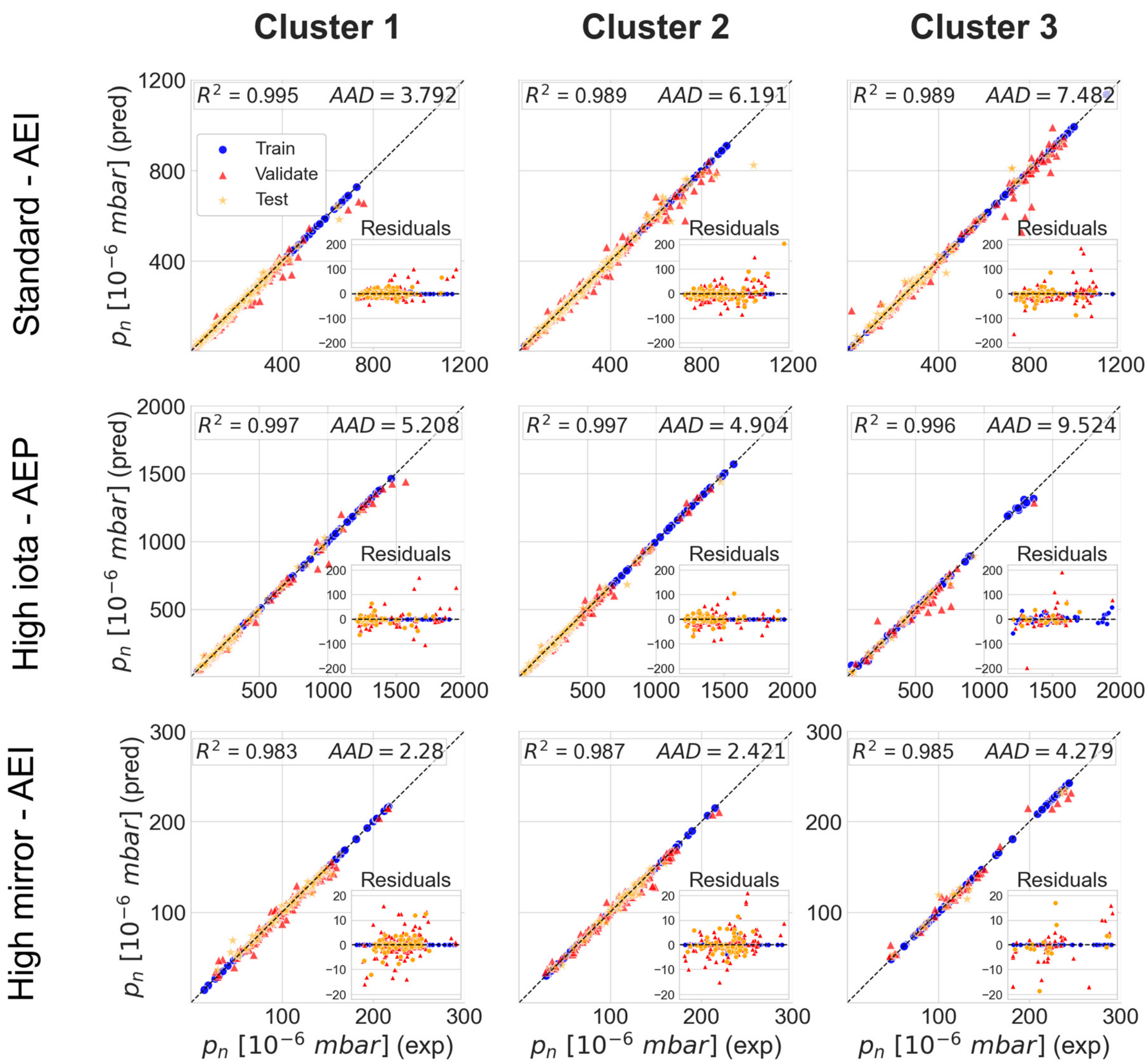

FIG. 6. Identity plots of the ET model trained on all investigated parameters for the standard, high iota and high mirror magnetic configurations, grouped by their respective f_{rad} clusters. In each case, the corresponding R^2 and AAD values of the test dataset are reported. The inset shows the residual plot ($y_i - \hat{y}_i$).

C. Predicted neutral gas pressure via the symbolic regression approach

As noted above, in contrast to ET, SR can show in a more straightforward manner the parameters that considers as most important, by incorporating them directly into the symbolic expressions. However, data dimensionality must remain low, since inclusion of many variables increases complexity and yields a non-manageable vast set of candidate equations. Thus, the present SR analysis is performed employing only the sets of important parameters.

In Ref. 23, where the effect of the plasma parameters [n_e, P_{heat}, f_{rad}, I_{tor}, T_c, T_e] on the neutral gas pressure p_n of W7-X for the standard, high iota and high mirror magnetic configurations, based on the SR approach, have been investigated, and the following two-parameter expressions:

$$p_n = \alpha_1 \, n_e^{\alpha_2} \, P_{heat}^{\alpha_3}, \tag{5}$$

have been proposed. For all cases considered, the values of the constants α, β, and c are provided in Table VII in Ref. 23.

Here, this analysis is repeated by employing the most influential parameters, defined in Table I, namely [n_e, P_{heat}, P_{rad}, I_{cc}] in the standard configuration and [n_e, P_{heat}, P_{rad}] in the high iota and high mirror configurations. For each of the nine datasets considered, the SR process (outlined in Sec. II) has been applied, performing numerous SR calculations, and the dominant expressions have been extracted. Then, by following the same strategy as in Ref. 23, i.e., by compromising between accuracy, complexity and generality, as well as expression form repeatability across different random states, the following closed form expressions are proposed for the estimation of p_n.

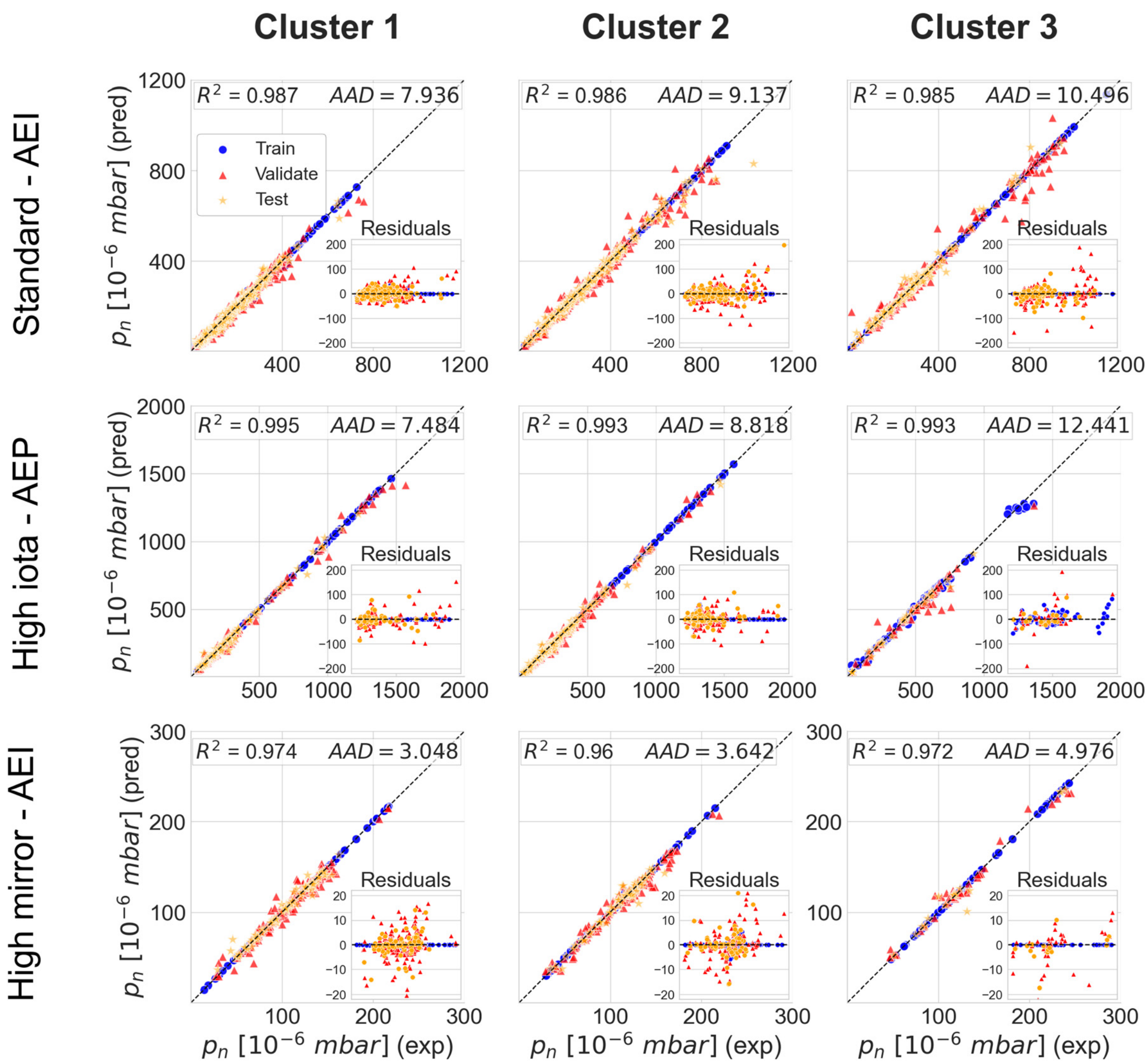

FIG. 7. Identity plots of the ET model trained only on the key parameters for the standard, high iota and high mirror magnetic configurations, grouped by their respective f_{rad} clusters. In each case, the corresponding R^2 and AAD values of the test dataset are reported. The inset shows the residual plot ($y_i - \hat{y}_i$).

In the standard configuration for all three clusters, the proposed expressions contain three parameters, namely, n_e, P_{heat}, and I_{cc}, and are given by

$$p_n = \alpha_1\, n_e^{\alpha_2}\, (P_{heat} + \alpha_3)^{\alpha_4}\, (I_{cc} + \alpha_5)^{\alpha_6}, \tag{6}$$

with the constants a_i, $i = 1, 2, \ldots 6$ being optimized to the specific cluster of f_{rad}. Their values can be found in Table II, represented in the 95% confidence interval format, as mentioned in Sec. II. In addition, in Table II, the two statistical measures of accuracy, R^2 and AAD, of the three-parameter expression (6), along with the corresponding accuracy metrics of the two-parameter expression (5),[23] are employed. Clearly, the present symbolic expressions, compared to the previous ones, demonstrate stronger performance, achieving values of R^2, higher than 0.9, with the corresponding AAD values also indicating minimal deviations from the actual measurements. Also, the three-parameter expressions (6) have closer resemblance with corresponding expressions, obtained via typical regression methods,[67] with the exception that they incorporate a correction factor added to the heating power. The importance of I_{cc}, which has been clearly shown via the feature importance and ET results, here is explicitly demonstrated in the SR expression. This is in good agreement with the experimental data,[34,35] as for positive values, strike lines move closer to the gaps, thereby enhancing p_n, while negative I_{cc} reduces p_n further, as the strike lines shift away.

In the high iota and high mirror configurations, although the associated six datasets are slightly different than the ones in Ref. 23, since the radiated power P_{rad} is explicitly included, the proposed SR expressions for all clusters considered are exactly the same as the two-parameter expressions (5), reported in Ref. 23. It is evident that, in all three magnetic configurations, SR does not favor expressions containing P_{rad}, or more precisely, the accuracy improvement obtained by

TABLE II. Standard configuration (AEI port) - constants α_i, $i = 1, 2, \ldots, 6$ of the SR expressions (6), with a 95% confidence interval, and the associated R^2 and AAD values.

	Equation (6) (present work)								Equation (5) (Ref. 23)	
Cluster	a_1	a_2	a_3	a_4	a_5	a_6	R^2	AAD	R^2	AAD
1	$4.34_{2.9}^{6.23}$	$1.15_{1.11}^{1.18}$	$0.25_{-0.53}^{3.13}$	$0.57_{0.38}^{0.82}$	$4.07_{3.28}^{4.81}$	$0.66_{0.53}^{0.77}$	0.93	18.850	0.91	21.612
2	$5.15_{2.85}^{10.0}$	$1.27_{1.2}^{1.32}$	$3.23_{1.84}^{4.64}$	$0.69_{0.53}^{0.8}$	$1.49_{0.34}^{3.34}$	$0.33_{0.15}^{0.61}$	0.92	32.511	0.87	40.545
3	$2.92_{2.4}^{3.83}$	$1.51_{1.38}^{1.65}$	$3.66_{3.08}^{4.75}$	$0.7_{0.57}^{0.85}$	$1.85_{0.37}^{3.06}$	$0.27_{0.12}^{0.4}$	0.92	36.927	0.89	42.020

including P_{rad} in the symbolic expressions is marginal. On the contrary, it always favors the inclusion of n_e and P_{heat} in all three magnetic configurations, as well as of I_{cc} in the standard configuration. It is noted that since the employed datasets of the high iota and high mirror configurations do not contain any current coil data dependency, it is not possible to examine, in these cases, the effect of I_{cc} on p_n. However, based on the results of the standard configuration, via the SR, as well as the ET models, the importance of I_{cc} in these two should be examined as soon as experimental data are available.

D. Comparison between extra trees and symbolic regression models

Here, a more thorough description on the effectiveness of the ET model and the SR two- and three-parameter expressions, defined in Eqs. (5) and (6) respectively, is performed by comparing directly with the experimental data (Fig. 8) and examining the relative error between predicted and actual data (Figs. 9 and 10). The comparison study is focused on the standard configuration and the ET predictions are made by harnessing only the information of the most important parameters (Table I).

In Fig. 8, the predicted and experimental neutral gas pressure p_n (y-axis) are plotted against the line integrated electron density n_e (x-axis), represented by different colors that depict the heating power P_{heat}. The comparison takes place for all ML models. Each one is trained and subsequently predicted p_n within its corresponding cluster and the predictions are then compiled and displayed in single figures.

All models capture the average trend of the experimental data, despite their significant scatter. The two-parameter SR expression [Fig. 8(a)] proposes a more compact behavior of p_n, whereas the three-parameter one [Fig. 8(b)] demonstrates a broader distribution of predictions that correspond more closely to the actual values [Fig. 8(d)]. Upon closer examination, the two-parameter expression exhibits a trend characterized by a sharper increase in p_n at high values of n_e and P_{heat} ($n_e > 9 \times 10^{19}$ m^{-2} and $P_{heat} > 3$ MW), while on the contrary, the three-parameter expression shows additional "behavior

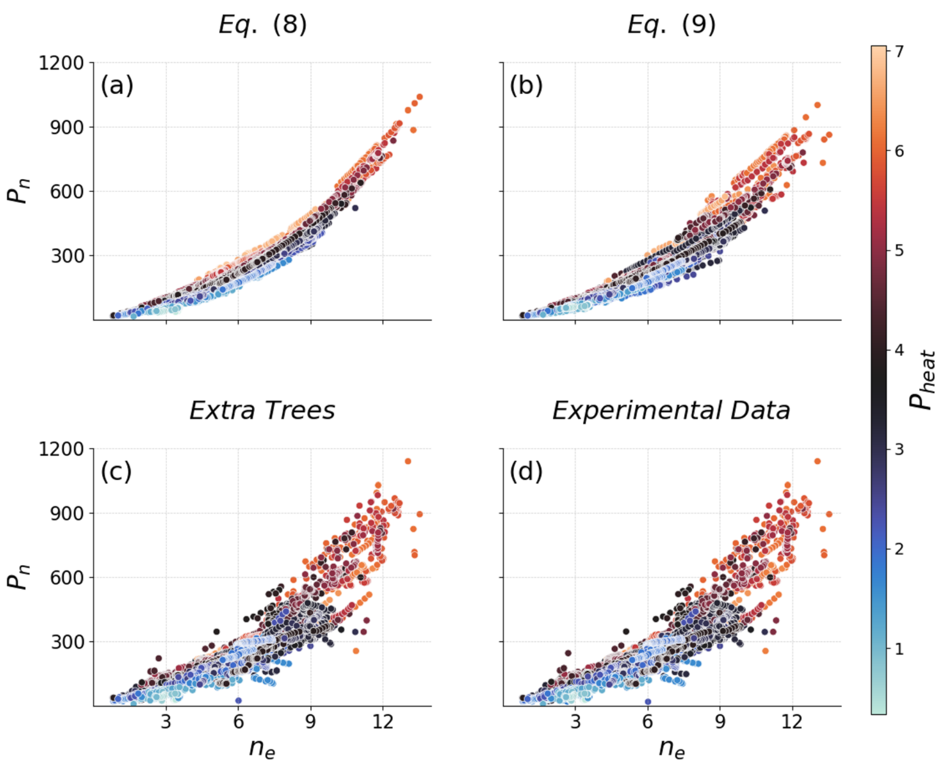

FIG. 8. Predicted and experimental neutral gas pressure p_n (y-axis) vs line integrated electron density n_e (x-axis), color-coded by heating power P_{heat} for the standard configuration; SR two-parameter expression (a), SR three-parameter expression (b), ET model (c), and experimental data (d).

streamlines" that maintain lower p_n levels at these instances, more closely to the actual data. Although this is not a concern within the investigated dataset, as the statistical error remains acceptable, it may pose problems when extrapolating p_n estimates to higher values of n_e and P_{heat}, as the two SR expressions may exhibit different behavior. Furthermore, predictions from the ET model [Fig. 8(c)] are highly accurate, exhibiting only minor inconsistencies, detectable through statistical measures but not easily visible to the naked eye.

In Fig. 9, the relative errors (RE) of the SR two- and three-parameter expressions and the ET model (y-axis) are provided against the actual values of p_n (x-axis). The RE are expressed as

$$RE = \frac{y_i - \hat{y}_i}{y_i} \times 100, \tag{7}$$

where y_i and $\hat{y}_i$ refer to the experimental and predicted pressure values, respectively. Columns represent the predictions on the corresponding f_{rad}, while rows represent the ML models. The horizontal lines in each plot represent prediction errors of 25%, 50%, and 100% and are included as visual guides, while the insets in each subfigure provide the number of data points within the corresponding relative error.

Across all three clusters and ML models, the majority of predictions fall within a 25% error range. Clearly, the relative errors on the ET model are significantly smaller than in the SR models. More specifically, in the ET model, the RE is larger than 25% in cluster 1 only for a very small number of points (46 out of 4406 data points), while in clusters 2 and 3 is, in most cases, much less than 25%. Comparing the relative errors between the SR models, in clusters 2 and 3, the three-parameter expression, as expected, clearly outperforms the two-parameter one. In cluster 1, the latter expression yields more predictions within the 25% error threshold than the former one, but this situation is reversed when the 50% error limit is considered. This may imply that the inclusion of I_{cc} in the closed form expressions is needed more in clusters 2 and 3, than in cluster 1, i.e., when $f_{rad} > 0.25$. This can be attributed to the fact that clusters 2 and 3 exhibit higher I_{cc} values than cluster 1 (as shown by the mean I_{cc} values in Table IV), which in turn indicates that the strike lines lie closer to the gaps.

It is also observed that, in general, the errors mostly occur at lower pressure values, where all three ML approaches consistently overestimate the predicted pressure. These very low pressures are probably of no practical interest. In contrast, at higher pressure readings, the errors of the SR expressions are reduced and tend to underestimate the true values, while the ET model consistently produces very accurate predictions.

To further investigate the behavior of the ML models in terms of the most important plasma parameters, in Fig. 10, the contour plots of the relative errors RE of all ML models are provided in a coordinate system with n_e in the x-axis and P_{heat} in the y-axis, color-coded by the magnitude of RE. The columns refer to cases $I_{cc} = [0, 1, 2]$, while the top three rows represent the ML models and the bottom row the actual data, where coloring accounts for the experimental p_n values.

The ET algorithm demonstrates negligible deviations from the actual data, as indicated by the black and dark red regions in Fig. 10 (excellent predictions). Compared to ET, the SR models demonstrate larger deviations from the actual data, as indicated by the bright red color (very good predictions), followed by a moderate amount of blue (good predictions) and a hint of yellow (relatively poor predictions). Clearly, the three-parameter expression outperforms the two-parameter one, since the yellow and blue regions are significantly reduced, particularly in the cases of $I_{cc} = [1, 2]$. In the case of $I_{cc} = 0$, the RE of the two SR expressions are close to each other, but the three-parameter expression still remains more reliable, since the bright red regions, compared to the blue ones, are reduced. In this case, the form of SR expressions (5) and (6) is very similar, and the better performance of Eq. (6) may be contributed to the correction factor α_3, which is added to P_{heat}. When $I_{cc} = 0$, the SR discrepancies are relatively small at moderate values of n_e and they increase at small and large values of n_e and this may be due to the larger number of data points encountered in moderate values of n_e, compared to the other two regions.

Closing this subsection, it is noted that although the ET model exhibits excellent accuracy on the training dataset it may struggle to generalize to unseen values, while the extrapolation capability of the SR predictions suggests that the expressions may capture, to a certain extent, the underlying physical mechanisms governing p_n.

IV. CONCLUDING REMARKS

The neutral gas pressure p_n in the sub-divertor of W7-X is predicted, via machine learning (ML), based on the actual data of seven plasma parameters of the OP1.2b experimental campaign for the standard, high iota and high mirror magnetic configurations. To better capture the changing behavior moving from attached to detached plasma conditions, the dataset in each configuration is divided into three clusters with regard to the fraction of radiated power f_{rad} resulting to nine datasets. The data are statistically analyzed by the Pearson coefficients and a feature importance analysis. The former one provides the pairwise relation of p_n with each of the plasma parameters, while the latter one clearly identifies, via the SHAP approach, the most important plasma parameters affecting the estimation of p_n. Then, p_n is predicted by two ML methods, namely, the extremely randomized trees (ET) and symbolic regression (SR) models. The effectiveness of the two ML models, which operate differently, is thoroughly examined by extensive comparisons between the estimated and actual values of the neutral gas pressure.

The feature importance analysis identifies, in the standard configuration, the parameters $[n_e, P_{heat}, P_{rad}, I_{cc}]$ and in the high iota and high mirror configurations, the parameters $[n_e, P_{heat}, P_{rad}]$ as the most influential ones. In all cases considered, the line integrated electron density n_e is ranked as the most dominant parameter, while the heating power P_{heat}, followed by the radiated power P_{rad}, are always included in the key parameters. In the standard configuration, when $f_{rad} > 0.25$, the coil control current I_{cc} has also been ranked very high, even higher than P_{heat} and close to n_e. Since the employed datasets of the high iota and high mirror configurations do not contain any current coil data, the effect of I_{cc} on p_n has not been considered. The other examined plasma parameters, which include the center and edge temperatures and the toroidal current, are always ranked at the end of the list and are considered as not so important.

By exploiting the capability of classical ML models to handle multidimensional data and identify complex interconnections within the input parameter space, the ET has been applied to deduce p_n, using all seven plasma parameters, as well as the most important ones. In both cases, almost perfect agreement with actual data is obtained, with the coefficient of determination $R^2 \geq 0.96$, confirming the expected ability

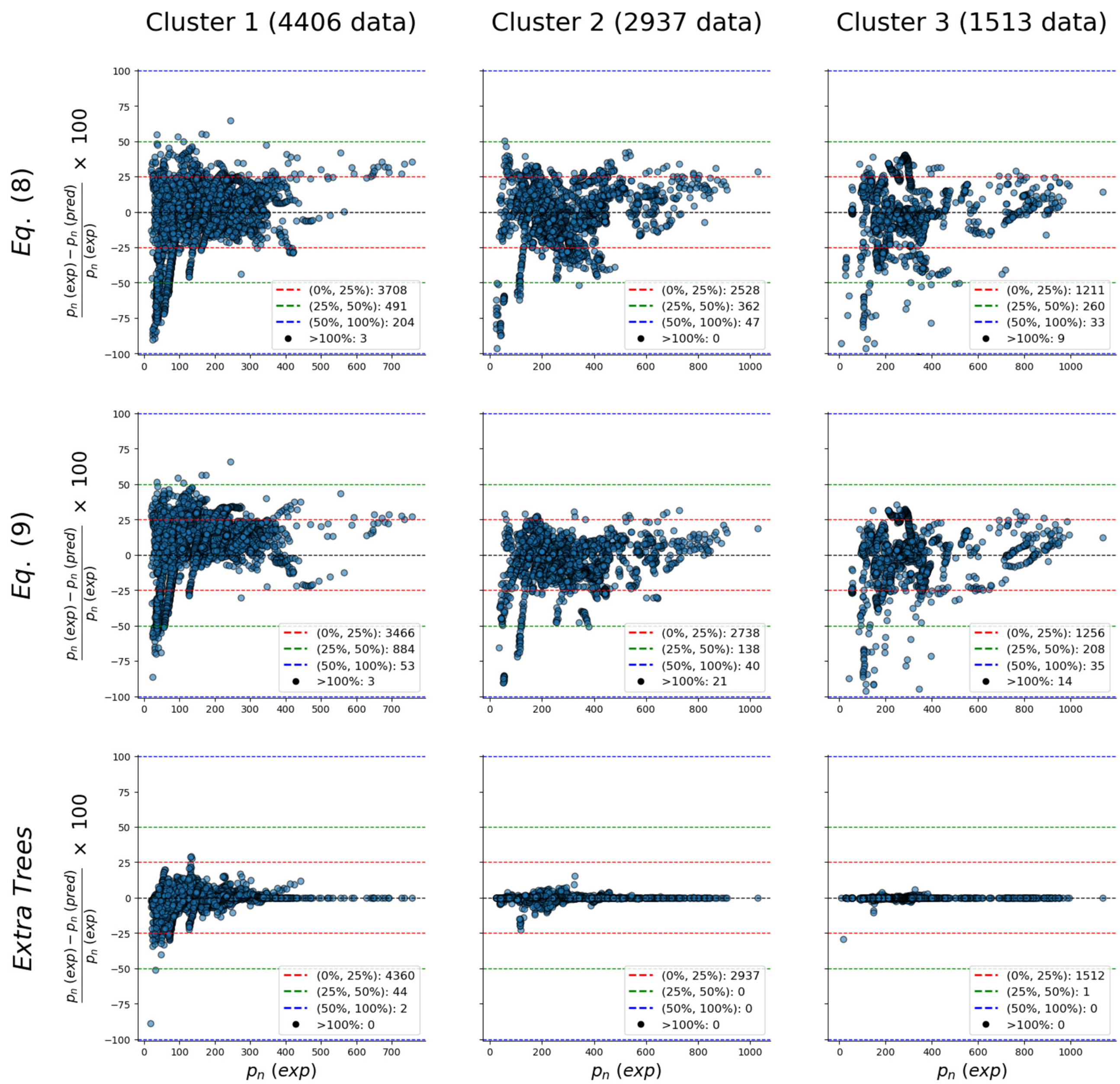

FIG. 9. Relative error *RE* (%) of ML models (*y*-axis) vs actual values of p_n (*x*-axis) for the standard configuration; columns correspond to the respective f_{rad} clusters, while rows represent the SR two- and three-parameter expressions and the ET model (trained on key parameters). Horizontal reference lines at 25% (red), 50% (green), and 100% (blue) errors serve as visual guides.

of the ET model to produce very accurate results and validating the selected key parameters. However, the ET model lacks interpretability behind its predictions and may struggle to generalize to unseen values. To overcome these pitfalls, the SR model is also applied to derive closed form expressions that correlate the investigated parameters.

The SR investigation is based only on the key parameters, since the data dimensionality must remain low to better exploit the method characteristics (e.g., clear connection between p_n and plasma parameters, extrapolation capability of its predictions, disclosing underlying physical mechanisms). The proposed closed form expressions in each magnetic configuration include [n_e, P_{heat}, I_{cc}] in the standard configuration and [n_e, P_{heat}] in the high iota and high mirror configurations (i.e., all associated key parameters, except P_{rad}, which consistently is not selected by SR). Although the

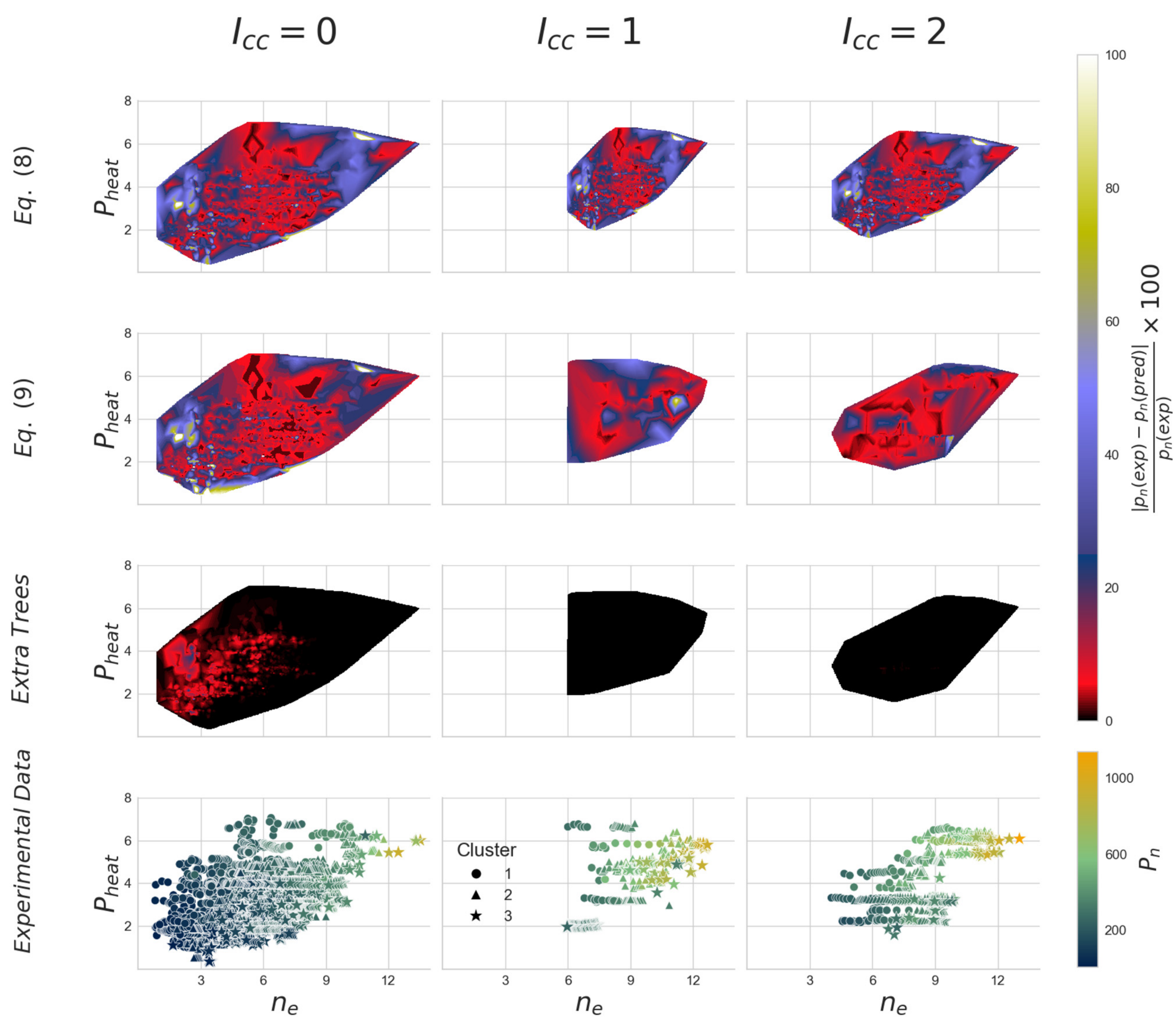

FIG. 10. Contour plots of relative error *RE* (%) of ML models for the standard configuration plotted on a coordinate system (n_e, P_{heat}) and color-coded by error percentage; columns correspond to $I_{cc} = [0, 1, 2]$, while rows represent the SR two- and three-parameter expressions, the ET model (trained on key parameters) and the experimental measurements.

p_n predictions of SR lag behind those of ET, they still demonstrate very good performance, with $R^2 \geq 0.92$. Here, the dependency of p_n on the plasma parameters is explicitly demonstrated in the SR expressions.

Furthermore, in the standard configuration, a detailed and thorough comparison of the p_n predictions, deduced by the ET model and the three-parameter closed form expression obtained by SR, is performed. The comparison also includes a previously obtained two-parameter SR expression,[23] which has been deduced using similar sets of parameters, but without the parameter I_{cc}. It has been found that all models capture the average trend of the experimental data. However, the two-parameter SR expression exhibits a compact pattern, whereas the three-parameter one demonstrates a disperse distribution of predictions that better represent the actual values and has greater potential for extrapolating to unseen p_n estimates. The ET model yields nearly perfect predictions from a statistical standpoint, with only minor deviations. Notably, in all models the majority of computed relative errors between actual and predicted data fall within a 25% threshold, with most of them occurring in the lower-pressure regime.

The present investigation provides valuable insights into the identification of the key plasma parameters affecting the sub-divertor neutral gas pressure and its very accurate prediction via the ET and SR methods, covering, in parallel, the positive and negative aspects of each of the employed ML approaches. The presented interconnection between the sub-divertor and plasma parameters and conditions, may support the design and optimization of the particle and impurity exhaust system of W7-X and other fusion reactors. Furthermore, the present work is broadening the scope of ML applications in fusion.

Future work will primarily focus on evaluating and refining the present study using the experimental data from W7-X OP2.2 and OP2.3 campaigns, which however still require some post-processing and validation before applied in ML studies. This constitutes a key step in calibrating the effectiveness of ET and SR predictions under different experimental conditions. Emphasis will be placed on improving the SR expressions, as they provide transparent and interpretable representation of the interdependencies among the investigated parameters. To do so, physical insights will be used not only as an expression selection criterion, but also as part of the training procedure. Furthermore, all aforementioned methodologies will be designed by using, not only *MSE*-based loss functions, but also physics-informed approaches that integrate partial differential equations and/or analytical expressions (e.g., the two-point model) directly into the loss function, thereby enhancing both accuracy and physical consistency of predictions.

ACKNOWLEDGMENTS

This work has been carried out within the framework of the EUROfusion Consortium, funded by the European Union via the

TABLE III. Range, mean and standard deviation of measured neutral gas pressure and plasma parameters for the standard (AEI port), high iota (AEH) and high mirror (AEI) configurations.

	p_n (10^{-6} mbar)	n_e (10^{19} m^{-2})	P_{heat} (MW)	P_{rad} (MW)	I_{tor} (kA)	I_{cc} (kA)	T_c (keV)	T_e (keV)
			Standard - AEI (No. of datapoints: 8856)					
Min	7.60	0.82	0.34	0.05	−2.73	−0.50	0.33	0.10
Max	1138.04	13.52	7.06	4.97	10.00	2.50	10.98	3.17
Mean	225.41	5.85	3.29	1.00	2.38	0.29	2.98	0.78
Std.	148.63	2.30	1.12	0.67	1.99	0.67	1.63	0.42
			High iota - AEP (No. of datapoints: 3797)					
Min	28.45	0.91	0.46	0.14	−3.33	0.00	0.28	0.18
Max	1568.78	12.02	6.24	3.16	1.70	0.00	11.57	2.72
Mean	251.29	4.56	2.31	0.74	−0.67	0.00	3.14	0.70
Std.	221.87	1.82	1.16	0.43	0.73	0.00	1.38	0.34
			High mirror - AEI (No. of datapoints: 1587)					
Min	14.16	1.38	0.75	0.20	−0.08	0.00	0.03	0.00
Max	245.16	8.21	5.26	3.35	7.93	0.00	9.04	1.34
Mean	111.17	4.34	2.91	0.85	1.25	0.00	3.81	0.62
Std.	36.26	1.19	0.90	0.44	0.93	0.00	1.46	0.18

TABLE IV. Range of measured neutral gas pressure and plasma parameters for the three f_{rad} clusters in standard configuration at the AEI port.

	p_n (10^{-6} mbar)	n_e (10^{19} m^{-2})	P_{heat} (MW)	P_{rad} (MW)	I_{tor} (kA)	I_{cc} (kA)	T_c (keV)	T_e (keV)
		Cluster 1 - $f_{rad} \in (0,\ 0.25)$				No. of datapoints: 4406		
Min	18.63	0.82	0.90	0.05	−0.15	−0.50	0.75	0.14
Max	756.93	10.58	7.06	1.67	10.00	2.50	10.98	3.17
Mean	157.39	4.55	3.26	0.55	3.06	0.14	3.78	0.95
Std.	97.04	1.84	1.11	0.24	2.22	0.51	1.66	0.45
		Cluster 2 - $f_{rad} \in (0.25,\ 0.50)$				No. of datapoints: 2937		
Min	23.19	1.87	0.37	0.17	−2.73	0.00	0.52	0.12
Max	1027.63	13.26	6.82	3.02	8.35	2.50	10.28	1.85
Mean	284.55	6.99	3.47	1.21	1.85	0.43	2.37	0.63
Std.	145.33	1.93	1.10	0.45	1.50	0.77	1.22	0.33
		Cluster 3 - $f_{rad} \in (0.50,\ 0.80)$				No. of datapoints: 1513		
Min	7.60	1.68	0.34	0.20	−1.32	0.00	0.33	0.10
Max	1138.04	13.52	6.25	4.97	7.45	2.50	6.94	1.62
Mean	308.72	7.44	3.05	1.91	1.39	0.45	1.84	0.55
Std.	183.61	1.98	1.15	0.77	1.24	0.76	0.91	0.24

Euratom Research and Training Programme (Grand Agreement No 101052200 - EUROfusion). Views and opinions expressed are however those of the author(s) only and do not necessarily reflect those of the European Union or the European Commission. Neither the European Union nor the European Commission can be held responsible for them. This work was supported by computational time granted from the EUROfusion HPC Marconi Fusion.

AUTHOR DECLARATIONS

Conflict of Interest

The authors have no conflicts to disclose.

Author Contributions

D. Angelis: Conceptualization (equal); Data curation (equal); Formal analysis (equal); Investigation (equal); Methodology (equal); Software (lead); Visualization (equal); Writing – original draft (equal). **F. Sofos:** Conceptualization (equal); Formal analysis (equal); Investigation (equal); Methodology (equal); Project administration (equal); Supervision (equal); Validation (equal); Visualization (equal); Writing – review & editing (equal). **S. Misdanitis:** Formal analysis (equal); Investigation (equal); Methodology (equal); Visualization (equal); Writing – original draft (equal). **C. Dritselis:** Investigation (equal); Methodology (equal); Visualization (equal); Writing – original draft (equal). **T. E. Karakasidis:** Formal analysis (equal); Validation (equal); Writing – review & editing (equal). **D. Valougeorgis:** Conceptualization (equal);

TABLE V. Range of measured neutral gas pressure and plasma parameters for the three f_{rad} clusters in high iota configuration at the AEP port.

	p_n (10^{-6} mbar)	n_e (10^{19} m^{-2})	P_{heat} (MW)	P_{rad} (MW)	I_{tor} (kA)	I_{cc} (kA)	T_c (keV)	T_e (keV)
		Cluster 1 - $f_{rad} \in (0,\ 0.30)$				No. of datapoints: 1442		
Min	44.37	0.91	0.58	0.14	−3.33	0.00	0.47	0.40
Max	1568.78	11.44	6.24	1.80	1.70	0.00	11.57	2.72
Mean	237.37	4.04	2.46	0.54	−0.57	0.00	3.56	0.93
Std.	248.82	2.03	1.34	0.33	0.81	0.00	1.44	0.41
		Cluster 2 - $f_{rad} \in (0.30,\ 0.50)$				No. of datapoints: 2061		
Min	28.45	1.68	0.46	0.15	−2.24	0.00	0.58	0.22
Max	1501.71	11.49	5.76	2.37	1.46	0.00	6.79	1.86
Mean	239.71	4.80	2.21	0.82	−0.75	0.00	2.91	0.53
Std.	156.65	1.23	0.89	0.36	0.63	0.00	1.16	0.15
		Cluster 3 - $f_{rad} \in (0.50,\ 0.80)$				No. of datapoints: 294		
Min	29.92	1.26	0.53	0.26	−2.80	0.00	0.28	0.18
Max	1365.28	12.02	5.10	3.16	0.84	0.00	6.43	1.19
Mean	396.95	6.27	2.14	1.24	−1.24	0.00	2.01	0.47
Std.	289.75	2.37	1.14	0.66	0.59	0.00	1.15	0.14

TABLE VI. Range of measured neutral gas pressure and plasma parameters for the three f_{rad} clusters in high mirror configuration at the AEI port.

	p_n (10^{-6} mbar)	n_e (10^{19} m^{-2})	P_{heat} (MW)	P_{rad} (MW)	I_{tor} (kA)	I_{cc} (kA)	T_c (keV)	T_e (keV)
		Cluster 1 - $f_{rad} \in (0,\ 0.30)$				No. of datapoints: 800		
Min	14.16	1.38	1.06	0.20	−0.05	0.00	0.03	0.00
Max	216.51	8.21	5.26	1.40	7.93	0.00	9.04	1.34
Mean	107.65	4.16	3.11	0.63	1.35	0.00	4.16	0.70
Std.	33.22	1.22	0.84	0.23	1.04	0.00	1.71	0.21
		Cluster 2 - $f_{rad} \in (0.30,\ 0.50)$				No. of datapoints: 428		
Min	28.90	1.92	0.75	0.33	−0.04	0.00	0.78	0.37
Max	219.42	7.15	4.78	2.20	3.70	0.00	5.25	0.76
Mean	110.62	4.39	2.65	1.01	1.12	0.00	3.49	0.55
Std.	34.78	1.11	0.85	0.34	0.79	0.00	0.97	0.05
		Cluster 3 - $f_{rad} \in (0.50,\ 0.80)$				No. of datapoints: 168		
Min	46.72	2.11	0.91	0.58	−0.08	0.00	1.19	0.41
Max	245.16	7.66	4.52	3.35	2.19	0.00	4.74	0.63
Mean	127.88	4.92	2.50	1.52	0.96	0.00	3.16	0.50
Std.	52.39	1.28	1.01	0.66	0.64	0.00	0.71	0.05

Formal analysis (equal); Funding acquisition (lead); Investigation (equal); Methodology (equal); Project administration (equal); Supervision (equal); Validation (equal); Visualization (equal); Writing – review & editing (equal). **V. Haak:** Data curation (equal); Investigation (supporting); Methodology (supporting). **D. Naujoks:** Investigation (supporting); Methodology (supporting); Project administration (equal); Supervision (equal); Validation (equal); Writing – review & editing (equal). **G. Schlisio:** Data curation (equal); Software (supporting). **S. A. Bozhenkov:** Data curation (equal); Software (supporting). **V. Perseo:** Data curation (equal); Software (supporting).

DATA AVAILABILITY

The data that support the findings of this study are available from the corresponding author upon reasonable request.

APPENDIX: EMPLOYED DATASETS OF THE W7-X OP1.2B CAMPAIGN

Table III provides the key statistics of the three datasets, along with the units of all measured quantities. Also, the number of data points in each of the three datasets is specified, with the standard, high iota and high mirror configurations counting 8856, 3787, and 1587 data. As it is well known, the highest pressures are in the high iota configuration, followed by the ones in the standard configuration, while the pressures in the high mirror configuration are significantly lower. Also, I_{cc} takes in the standard configuration the values $[-0.5, 0, \ldots, 2.5]$ while in the high iota and high mirror configurations always $I_{cc} = 0$ (not available data for $I_{cc} \neq 0$) and therefore, its effect on p_n is examined only in the former case. Additionally, Tables IV–VI shows characteristics and statistics of the nine datasets (three clusters for each magnetic configuration) employed in the present work.

REFERENCES

[1]W. H. Patrick, *Artificial Intelligence* (Addison-Wesley, 1992).
[2]S. Raschka, *Python Machine Learning* (Packt Publishing Ltd, 2015).
[3]A. Pavone, A. Merlo, S. Kwak, and J. Svensson, "Machine learning and Bayesian inference in nuclear fusion research: An overview," Plasma Phys. Controlled Fusion **65**(5), 053001 (2023).
[4]S. Dasbach and S. Wiesen, "Towards fast surrogate models for interpolation of tokamak edge plasmas," Nucl. Mater. Energy **34**, 101396 (2023).
[5]S. K. Kim, R. Shousha, S. M. Yang, Q. Hu, S. H. Hahn, A. Jalalvand, J.-K. Park, N. C. Logan, A. O. Nelson, Y.-S. Na *et al.*, "Highest fusion performance without harmful edge energy bursts in tokamak," Nat. Commun. **15**(1), 3990 (2024).
[6]P. Ga˛sior, M. Kastek, M. Ladygina, and D. Sokulski, "ANN based LIBS models for quasi-experimental spectra relevant for materials for next-step fusion reactors," Phys. Plasmas **31**(5), 052507 (2024).
[7]V. Gopakumar, S. Pamela, L. Zanisi, Z. Li, A. Gray, D. Brennand, N. Bhatia, G. Stathopoulos, M. Kusner, M. P. Deisenroth *et al.*, "Plasma surrogate modelling using Fourier neural operators," Nucl. Fusion **64**(5), 056025 (2024).
[8]S. Chouchene, F. Brochard, N. Lemoine, J. Cavalier, M. Desecures, and V. Weinzettl, "Mutual interactions between plasma filaments in a tokamak evidenced by fast imaging and machine learning," Phys. Rev. E **109**(4), 045201 (2024).
[9]E. Grelier, R. Mitteau, and V. Moncada, "Deep learning-based process for the automatic detection, tracking, and classification of thermal events on the in-vessel components of fusion reactors," Fusion Eng. Des. **192**, 113636 (2023).
[10]C. Staron, H. Le Borgne, R. Mitteau, E. Grelier, and N. Allezard, "Detection of thermal events by semi-supervised learning for tokamak first wall safety," IEEE Trans. Instrum. Meas. **73**, 1–9 (2024).
[11]S. Kajita, D. Nishijima, K. Fujii, H. Tanaka, J. Vernimmen, H. van der Meiden, I. Classen, and N. Ohno, "Machine learning aided line intensity ratio method for helium–hydrogen mixed recombining plasmas," Plasma Phys. Controlled Fusion **66**(10), 105005 (2024).
[12]S. Cai, Z. Mao, Z. Wang, M. Yin, and G. E. Karniadakis, "Physics-informed neural networks (PINNs) for fluid mechanics: A review," Acta Mech. Sin. **37**(12), 1727–1738 (2021).
[13]E. Aymerich, F. Pisano, B. Cannas, G. Sias, A. Fanni, Y. Gao, D. Böckenhoff, and M. Jakubowski, "Physics informed neural networks towards the real-time calculation of heat fluxes at W7-X," Nucl. Mater. Energy **34**, 101401 (2023).
[14]A. Mathews, M. Francisquez, J. W. Hughes, D. R. Hatch, B. Zhu, and B. N. Rogers, "Uncovering turbulent plasma dynamics via deep learning from partial observations," Phys. Rev. E **104**(2), 025205 (2021).
[15]A. Mathews, N. Mandell, M. Francisquez, J. W. Hughes, and A. Hakim, "Turbulent field fluctuations in gyrokinetic and fluid plasmas," Phys. Plasmas **28**(11), 112301 (2021).
[16]K. Prantikos, S. Chatzidakis, L. H. Tsoukalas, and A. Heifetz, "Physics-informed neural network with transfer learning (TL-PINN) based on domain similarity measure for prediction of nuclear reactor transients," Sci. Rep. **13**(1), 16840 (2023).
[17]J. Dong, J. Li, Y. Ding, X. Zhang, N. Wang, D. Li, W. Yan, C. Shen, Y. He, X. Ren *et al.*, "Machine learning application to predict the electron temperature on the J-TEXT tokamak," Plasma Sci. Technol. **23**(8), 085101 (2021).
[18]G. Holt, A. Keats, S. Pamela, M. Kryjak, A. Agnello, N. Amorisco, B. Dudson, and M. Smyrnakis, "Tokamak divertor plasma emulation with machine learning," Nucl. Fusion **64**(8), 086009 (2024).
[19]J. Seo, S. Kim, A. Jalalvand, R. Conlin, A. Rothstein, J. Abbate, K. Erickson, J. Wai, R. Shousha, and E. Kolemen, "Avoiding fusion plasma tearing instability with deep reinforcement learning," Nature **626**(8000), 746–751 (2024).
[20]A. Murari, E. Peluso, T. Craciunescu, S. Dormido-Canto, M. Lungaroni, R. Rossi, L. Spolladore, J. Vega, M. Gelfusa, and J. Contributors, "Frontiers in data analysis methods: From causality detection to data driven experimental design," Plasma Phys. Controlled Fusion **64**(2), 024002 (2022).
[21]C. S. Chang, S. Ku, R. Hager, R. M. Churchill, J. Hughes, F. Köchl, A. Loarte, V. Parail, and R. A. Pitts, "Constructing a new predictive scaling formula for ITER's divertor heat-load width informed by a simulation-anchored machine learning," Phys. Plasmas **28**(2), 022501 (2021).
[22]A. Murari, E. Peluso, J. Vega, J. García-Regaña, J. Velasco, G. Fuchert, and M. Gelfusa, "Scaling laws of the energy confinement time in stellarators without renormalization factors," Nucl. Fusion **61**(9), 096036 (2021).
[23]D. Angelis, F. Sofos, S. Misdanitis, C. Dritselis, T. E. Karakasidis, D. Valougeorgis, V. Haak, D. Naujoks, G. Schlisio, S. A. Bozhenkov *et al.*, "Data driven prediction of the neutral gas pressure in the stellarator Wendelstein 7-X," Plasma Phys. Controlled Fusion **67**(7), 075004 (2025).
[24]M. Brenzke, S. Wiesen, M. Bernert, D. Coster, J. Jitsev, Y. Liang, U. von Toussaint, A. U. Team, and E. M. Team, "Divertor power load predictions based on machine learning," Nucl. Fusion **61**(4), 046023 (2021).
[25]A. Agrawal and A. Choudhary, "Perspective: Materials informatics and big data: Realization of the "fourth paradigm" of science in materials science," APL Mater. **4**(5), 053208 (2016).
[26]A. Kallenbach, H. J. Sun, T. Eich, D. Carralero, J. Hobirk, A. Scarabosio, M. Siccinio, A. U. team, and E. M. team, "Parameter dependences of the separatrix density in nitrogen seeded ASDEX Upgrade H-mode discharges," Plasma Phys. Controlled Fusion **60**(4), 045006 (2018).
[27]J. You, G. Mazzone, E. Visca, H. Greuner, M. Fursdon, Y. Addab, C. Bachmann, T. Barrett, U. Bonavolontà, B. Böswirth *et al.*, "Divertor of the European DEMO: Engineering and technologies for power exhaust," Fusion Eng. Des. **175**, 113010 (2022).
[28]V. Haak, S. A. Bozhenkov, Y. Feng, A. Kharwandikar, T. Kremeyer, D. Naujoks, V. Perseo, G. Schlisio, U. Wenzel, and the W7-X Team, "Overview over the neutral gas pressures in Wendelstein 7-X during divertor operation under boronized wall conditions," Plasma Phys. Controlled Fusion **65**(5), 055024 (2023).
[29]V. Haak, C. Dhard, D. Boeyaert, T. Bräuer, V. Bykov, C. Day, S. Degenkolbe, G. Ehrke, J. Igitkhanov, M. Khokhlov *et al.*, "First operation and validation of simulations for the divertor cryo-vacuum pump in Wendelstein 7-X," Fusion Eng. Des. **208**, 114671 (2024).

[30]U. Wenzel, G. Motojima, M. Kobayashi, M. Goto, Y. Hayashi, S. Masuzaki, G. Kawamura, B. Jagielski, and V. Haak, "Ultrahigh neutral pressures in the subdivertor of the large helical device," Nucl. Fusion **64**(3), 034002 (2024).
[31]S. Varoutis, C. Tantos, H. Strobel, D. Boeyaert, Y. Igitkhanov, F. Litovoli, C. Dhard, V. Haak, D. Naujoks, and the W7-X Team, "Numerical analysis of gas exhaust in Wendelstein 7-X using the direct simulation Monte Carlo method," Nucl. Fusion **65**(7), 076001 (2025).
[32]P. Geurts, D. Ernst, and L. Wehenkel, "Extremely randomized trees," Mach. Learn. **63**(1), 3–42 (2006).
[33]D. Angelis, F. Sofos, and T. E. Karakasidis, "Artificial intelligence in physical sciences: Symbolic regression trends and perspectives," Arch. Comput. Methods Eng. **30**(6), 3845–3865 (2023).
[34]M. Sleczka, M. Jakubowski, A. Ali, P. Drewelow, Y. Gao, H. Niemann, M. Otte, A. Puig Sitjes, G. Wurden *et al.*, "Modulation of the strike line position using control coils in Wendelstein 7-X," in *45th EPS Conference on Plasma Physics* (European Physical Society, 2018).
[35]F. Pisano, B. Cannas, A. Fanni, G. Sias, Y. Gao, M. Jakubowski, H. Niemann, A. Puig Sitjes, and W.-X. Team, "Learning control coil currents from heat-flux images using convolutional neural networks at Wendelstein 7-X," Plasma Phys. Controlled Fusion **63**(2), 025009 (2021).
[36]T. Sunn Pedersen, A. Dinklage, Y. Turkin, R. Wolf, S. Bozhenkov, J. Geiger, G. Fuchert, H.-S. Bosch, K. Rahbarnia, H. Thomsen *et al.*, "Key results from the first plasma operation phase and outlook for future performance in Wendelstein 7-X," Phys. Plasmas **24**(5), 055503 (2017).
[37]Y. Gao, J. Geiger, M. W. Jakubowski, P. Drewelow, M. Endler, K. Rahbarnia, S. Bozhenkov, M. Otte, Y. Suzuki, Y. Feng *et al.*, "Effects of toroidal plasma current on divertor power depositions on Wendelstein 7-X," Nucl. Fusion **59**(10), 106015 (2019).
[38]S. A. Lazerson, Y. Gao, K. Hammond, C. Killer, G. Schlisio, M. Otte, C. Biedermann, M. Spolaore, S. Bozhenkov, J. Geiger *et al.*, "Tuning of the rotational transform in Wendelstein 7-X∗," Nucl. Fusion **59**(12), 126004 (2019).
[39]M. Jakubowski, M. Endler, Y. Feng, Y. Gao, C. Killer, R. König, M. Krychowiak, V. Perseo, F. Reimold, O. Schmitz *et al.*, "Overview of the results from divertor experiments with attached and detached plasmas at Wendelstein 7-X and their implications for steady-state operation," Nucl. Fusion **61**(10), 106003 (2021).
[40]O. Schmitz, Y. Feng, M. Jakubowski, R. König, M. Krychowiak, M. Otte, F. Reimold, T. Barbui, C. Biedermann, S. Bozhenkov *et al.*, "Stable heat and particle flux detachment with efficient particle exhaust in the island divertor of Wendelstein 7-X," Nucl. Fusion **61**(1), 016026 (2020).
[41]G. Schlisio, U. Wenzel, D. Naujoks, T. Pedersen, H. Grote, V. Winters, H. Niemann, M. Mulsow, M. Krychowiak, P. Drewelow *et al.*, "The evolution of the bound particle reservoir in Wendelstein 7-X and its influence on plasma control," Nucl. Fusion **61**(3), 036031 (2021).
[42]T. Kremeyer, R. König, S. Brezinsek, O. Schmitz, Y. Feng, V. Winters, L. Rudischhauser, B. Buttenschön, K. Brunner, P. Drewelow *et al.*, "Analysis of hydrogen fueling, recycling, and confinement at Wendelstein 7-X via a single-reservoir particle balance," Nucl. Fusion **62**(3), 036023 (2022).
[43]U. Wenzel, G. Schlisio, P. Drewelow, M. Krychowiak, R. König, T. Pedersen, S. Bozhenkov, V. Haak, A. Kharwandikar, S. Lazerson *et al.*, "Gas exhaust in the Wendelstein 7-X stellarator during the first divertor operation," Nucl. Fusion **62**(9), 096016 (2022).
[44]S. Varoutis, C. Tantos, H. Strobel, C. Day, C. Dhard, V. Haak, Y. Igitkhanov, D. Naujoks, and the W7-X Team, "Numerical simulation of neutral gas dynamics in the W7-X sub-divertor," Nucl. Fusion **64**(7), 076011 (2024).
[45]F. Zinzendoff Okwonu, B. Laro Asaju, and F. Irimisose Arunaye, "Breakdown analysis of pearson correlation coefficient and robust correlation methods," IOP Conf. Ser.: Mater. Sci. Eng. **917**(1), 012065 (2020).
[46]Y. Feng, M. Kobayashi, T. Lunt, and D. Reiter, "Comparison between stellarator and tokamak divertor transport," Plasma Phys. Controlled Fusion **53**(2), 024009 (2011).
[47]J. Neter, W. Wasserman, and M. H. Kutner, *Applied Linear Regression Models* (Richard D. Irwin, 1983).
[48]S. Chatterjee and A. S. Hadi, *Regression Analysis by Example* (John Wiley & Sons, 2015).
[49]K. Papastamatiou, F. Sofos, and T. E. Karakasidis, "Machine learning symbolic equations for diffusion with physics-based descriptions," AIP Adv. **12**(2), 025004 (2022).
[50]V. K. Ayyadevara, *Pro Machine Learning Algorithms: A Hands-On Approach to Implementing Algorithms in Python and R*, 1st ed. (Apress, Berkeley, CA, 2018), Vol. XXI, p. 372.
[51]F. Sofos, C. Stavrogiannis, K. K. Exarchou-Kouveli, D. Akabua, G. Charilas, and T. E. Karakasidis, "Current trends in fluid research in the era of artificial intelligence: A review," Fluids **7**(3), 116 (2022).
[52]V. John, Z. Liu, C. Guo, S. Mita, and K. Kidono, "Real-Time lane estimation using deep features and extra trees regression," in *Image and Video Technology*, edited by T. Bräunl, B. Mc-Cane, M. Rivera, and X. Yu (Cham, Springer International Publishing, 2016), pp. 721–733.
[53]M. Stone, "Cross-validatory choice and assessment of statistical predictions," J. R. Stat. Soc.: Ser. B (Methodol.) **36**(2), 111–133 (1974).
[54]J. R. Koza, "Genetic programming as a means for programming computers by natural selection," Stat. Comput. **4**(2), 87–112 (1994).
[55]D. Wadekar, F. Villaescusa-Navarro, S. Ho, and L. Perreault-Levasseur, "Modeling assembly bias with machine learning and symbolic regression," arXiv:2012.00111 (2020).
[56]M. Cranmer (2020). "PySR: Fast & parallelized symbolic regression in Python/Julia," Zenodo. https://doi.org/10.5281/zenodo.4041459
[57]M. Cranmer, "Interpretable machine learning for science with PySR and SymbolicRegression.jl," arXiv:2305.01582 (2023).
[58]G. James, D. Witten, T. Hastie, R. Tibshirani *et al.*, *An Introduction to Statistical Learning* (Springer, 2013), Vol. 112, p. 1.
[59]P. Lemos, N. Jeffrey, M. Cranmer, S. Ho, and P. Battaglia, "Rediscovering orbital mechanics with machine learning," Mach. Learn: Sci. Technol. **4**(4), 045002 (2023).
[60]P. Virtanen, R. Gommers, T. E. Oliphant, M. Haberland, T. Reddy, D. Cournapeau, E. Burovski, P. Peterson, W. Weckesser, J. Bright *et al.*, "SciPy 1.0: Fundamental algorithms for scientific computing in Python," Nat. Methods **17**(3), 261–272 (2020).
[61]S. Silva, L. Vanneschi, A. I. Cabral, and M. J. Vasconcelos, "A semi-supervised Genetic Programming method for dealing with noisy labels and hidden overfitting," Swarm Evol. Comput. **39**, 323–338 (2018).
[62]M. O'Neill, L. Vanneschi, S. Gustafson, and W. Banzhaf, "Open issues in genetic programming," Genet. Program. Evolvable Mach. **11**(3), 339–363 (2010).
[63]S. M. Lundberg and S.-I. Lee, "A unified approach to interpreting model predictions," in *Advances in Neural Information Processing Systems*, edited by I. Guyon, U. V. Luxburg, S. Bengio, H. Wallach, R. Fergus, S. Vishwanathan, and R. Garnett (Curran Associates, Inc., 2017), Vol. 30.
[64]D. Wang, S. Thunéll, U. Lindberg, L. Jiang, J. Trygg, and M. Tysklind, "Towards better process management in wastewater treatment plants: Process analytics based on SHAP values for tree- based machine learning methods," J. Environ. Manage. **301**, 113941 (2022).
[65]Y. Meng, N. Yang, Z. Qian, and G. Zhang, "What makes an online review more helpful: An interpretation framework using XGBoost and SHAP values," J. Theor. Appl. Electron. Res. **16**(3), 466–490 (2020).
[66]A. V. Ponce-Bobadilla, V. Schmitt, C. S. Maier, S. Mensing, and S. Stodtmann, "Practical guide to SHAP analysis: Explaining supervised machine learning model predictions in drug development," Clin. Transl. Sci. **17**(11), e70056 (2024).
[67]F. Reimold, "Power and particle exhaust limitations in W7-X and its relation to density build-up in the divertor," paper presented at 26th International Conference on Plasma Surface Interaction in Controlled Fusion Devices (PSI 26), Marseille, France, 2024, see https://hdl.handle.net/21.11116/0000-000F-4881-E.